X-ray Phase Contrast and Absorption Imaging for the Quantification of Transient Cavitation in High-speed Nozzle Flows

I.K. Karathanassis[1,2,*,†], M. Heidari-Koochi[1,†], Q. Zhang[3], J. Hwang[4], P. Koukouvinis[1,2], J. Wang[3], M. Gavaises[1]

[1]School of Mathematics, Computer Science and Engineering, City, University of London, EC1V 0HB London, UK
[2]Combustion Research Facility, Sandia National Laboratories, Livermore, CA 94550, USA
[3]Advanced Photon Source, Argonne National Laboratory, Lemont, IL 60439, USA
[4]Centre for Advanced Vehicular Systems (CAVS), Department of Mechanical Engineering, Mississippi State University, Starkville, Mississippi, MS 39762, USA

[*]Corresponding author: ioannis.karathanassis@city.ac.uk
[†]Authors have contributed equally to the article

Abstract. High-flux synchrotron radiation has been employed in a time-resolved manner to characterise the distinct topology features and dynamics of different cavitation regimes arising in a throttle orifice with an abrupt flow-entry contraction. Radiographs obtained though both X-ray phase-contrast and absorption imaging have been captured at 67,890 frames per second. The flow lied in the turbulent regime (Re=35,500), while moderate (CN=2.0) to well-established (CN=6.0) cavitation conditions were examined encompassing the cloud and vortical cavitation regimes with pertinent transient features, such as cloud-cavity shedding. X-ray Phase-Contrast Imaging (XPCI), exploiting the shift in the X-ray wave phase during interactions with matter, offers sharp-refractive index gradients in the interface region. Hence, it is suitable for capturing fine morphological fluctuations of transient cavitation structures. Nevertheless, the technique cannot provide information on the quantity of vapour within the orifice. Such data have been obtained utilising absorption imaging, where beam attenuation is not associated with scattering and refraction events, and hence can be explicitly correlated with the projected vapour thickness in line-of-sight measurements. A combination of the two methods is proposed, as it has been found is capable of quantifying the vapour content arising in the complex nozzle flow, while also faithfully illustrating the dynamics of the highly-transient cavitation features.

Keywords: synchrotron radiation, time-resolved measurements, vapour quantification, compressible flow, fuel injectors

1. Introduction

The manifestation, development and collapse of cavitation bubbles can influence in a profound manner a plethora of natural and man-made flow processes at various length and time scales. Cavitation, either acoustic or inertial, control designates the quality and effectiveness of a wide range of biomedical applications with reference to sanitation, histotripsy/lithotripsy and focused ultrasound devices, mechanical heart valves [1,2]. The same applies to industrial practices relevant to the design of turbomachinery blades, ship propellers, high-pressure pumps, fuel injectors, rocket engines, inkjet printers and cleaning applications [3–5]. Onset of cavitation is accompanied by bubble and shockwave dynamics that can be manipulated to have attractive after-effects from a technological standpoint, e.g. to induce fragmentation of soft and solid matter, particle/deposits de-agglomeration

and spray atomisation [6–8]. However, the formation and collapse of vapour bubbles in an uncontrollable manner is associated numerous consequences, such as flow-performance unsteadiness, vibrations [9,10], noise [11,12] and material erosion [13,14].

Referring especially to inertial cavitation arising in turbulent liquid flows, its occurrence signifies the presence of a recirculating-flow pattern of considerable magnitude, which forces the local pressure to locally drop below the liquid saturation pressure, hence causing vapour bubbles to nucleate. A broad categorisation of cavitation regimes demonstrating a distinct transient nature should, in general, encompass cloud and vortical cavitation. The former regime manifests itself in the form of vapour pockets attached or near solid boundaries, usually due to the presence of adverse pressure gradients leading to flow separation [15]. The latter emerges owing to coherent vortex roll-up extending significantly within the flow core and exhibits an elongated or horse-shoe type shape. The overall topology and dynamics of partial and vortical cavities have been visualised with reference to a range of benchmark geometrical layouts such as hydrofoils, wedges and forward facing steps [16–22], converging diverging or throttle nozzles [23] and bluff bodies or obstacles [24–28].

Distinct mechanisms have been identified as responsible for conveying an unsteady behaviour to partial cavities accompanied by shedding of coherent vaporous structures [29,30]. The, so called, re-entrant jet constitutes the prevalent mechanism leading to partial-cavity break up, according to which flow-motion induced by the presence of an adverse pressure gradient with direction opposite the main flow interacts with the attached vapour pocket and severs large-scale structures. Two variations of the mechanism have been proposed [25]. Namely, for a ‘thin’ jet, a periodic shedding of coherent bubbly structures evolves, while on the contrary if the jet and cavity thicknesses are comparable, break-up occurs at several arbitrary locations, leading to chaotic shedding of small-scale structures. More recently, a second mechanism has been verified to cause pinch-off of vaporous clouds in different flow-layouts, with the specific process being governed by the propagation of a shockwave in the bubbly mixture rather than flow dynamics [16]. Information on the magnitude of underlying vortical motion can also be extracted by morphological fluctuations of elongated vortical cavities [31]. Choi et al. [32] have verified that, during the growth phase of a cavity forming in the core of a longitudinal vortex, its radius oscillation frequency scales with the single-phase vortex maximum tangential velocity.

Optical imaging with diffuse light has been conventionally employed to illustrate cavitation evolution and collapse in either wall-bounded or unconfined cavitating flows. The specific visualisation technique offers valuable information regarding the overall extent and morphology of vapour pockets, as well as distinct transient features of the two-phase field. Nevertheless, the use of visible light is associated with certain practical and fundamental limitations. Firstly, optical access to the flow-field must be ensured, a necessity that can pose major limitations for internal flows since transparent replicas of the actual flow devices must be fabricated with comparable refractive indices to the working fluids. Moreover, owing to the strong interaction of light with matter, the presence of relatively minor amounts of vapour can lead to considerable light scattering. This shortcoming is particularly crucial with reference to microfluidics devices comprising narrow flow passages, where cavitation topology can be highly complex with a multitude of transient features that can potentially render the entire active window opaque. Notwithstanding these weak points, the most prominent drawback of optical imaging is its complete inability to offer insight on the actual quantity of vapour present in the region of visualisation.

X-ray imaging has gained momentum in the last two decades as a technique capable of overcoming the limitations of optical imaging [33–35]. Flow visualisation techniques using X-rays can be broadly differentiated depending whether the contrast in the obtained radiographs results due to a reduction in the X-ray wave amplitude or a shift in its phase. The former technique is commonly referred to as absorption imaging and can offer quantitative information on the composition of the two-phase mixture. The latter is known as X-ray Phase Contrast Imaging (XPCI) which, although in essence remains a qualitative method, provides information on the volumetric topology of visualised cavities, taking advantage of the weak matter-induced X-ray scattering (the respective refractive index is much smaller compared to light). Stutz and Legoupil [22] were among the first to attempt time resolved,

vapour void-fraction measurements of cavitating flow utilising X-ray absorption. They visualised the unsteady cavity forming at the apex of a planar constriction at 1,000 frames per second (fps) and managed to capture the periodic shedding sequence in their volume-fraction data. Coutier-Delgosha et al. [36] utilised a similar X-ray imaging set-up with the same temporal resolution to obtain instantaneous void-fraction measurements within a sheet cavity emerging on the suction side of a two-dimensional hydrofoil. Aeschlimann et al. [37] obtained quantitative data regarding the vapour content of cross-flow cavitating vortices arising in a turbulent mixing layer with a temporal resolution up to 20,000 fps for spatial resolution of 1.5mm/pixel. They identified that the vapour pockets are a consequence of Kelvin-Helmholtz instabilities growing in the shear layer and determined their prevailing shedding frequency base on the obtained X-ray data.

The X-ray facility developed at the University of Michigan, which employs a cone-beam source [38] and can achieve a temporal resolution up to 1,000 fps for a spatial resolution of 0.125 mm/pixel has been employed in several studies, shedding light on the composition and dynamics of partial cavities arising in different benchmark geometries. For instance Ganesh et al. [16], utilising time-resolved void-fraction measurements, identified the bubbly-shock mechanism responsible for cloud cavitation break-up in a planar wedge-like constriction. In a subsequent investigation Wu et al. [20] elucidated the shedding dynamics, owing to the same mechanism, of partial cavities forming on a hydrofoil. More recently, Barbaca et al. [25] investigated the unsteady behaviour of both natural and ventilated cavities past a two-dimensional obstacle. A combination of diffuse-light imaging and X-ray absorption measurements, verified the presence of two regimes depending on the re-entrant jet to cavity thickness ratio, as discussed earlier in this section.

X-ray absorption imaging can be extended to a computed-tomography (CT) reconstruction, which provides quantitative information for the entire volume of the visualised flow path, rather than projected values, as is the case for line-of-sight methods discussed so far. With the use of a laboratory-scale, cone-beam X-ray source Mitroglou et al. [39] obtained time-averaged, volumetric quantitative data of the cloud cavity arising within a millimetre-sized nozzle, resembling a heavy-duty fuel injector. Due to the time-averaged nature of the data, no transient features could be captured. Bauer et al. [40] performed CT scanning of the two-phase flow field in an orifice with the same design rationale as [39], yet with characteristic dimensions of the order of centimetres. A CT facility employing a moving X-ray source was utilised, capable of obtaining cross-flow slices at different locations along the flow path with a spatial resolution of 1mm. Frame rates up to 8,000 fps were achieved for each irradiated slice having a thickness of 1 mm, hence the dynamically-evolving cavitating flow could be quantified to some extent. Finally, Dash et al. [41] used a medical-type CT setup to obtain the time-averaged, three-dimensional void fraction distribution of the transient two-phase mixture arising at the throat of a axisymmetric converging-diverging nozzle.

Synchrotron radiation offers a parallel beam of much higher flux compared to laboratory scale-sources, which can also be collimated to a narrow X-ray energy spectrum, thus alleviating the beam-hardening influence on flow quantification. Beam hardening refers to the shift to higher average energy of polychromatic beams after interaction with matter due to the selective absorption of low-energy photons, an intrinsically undesirable phenomenon resulting to reduced accuracy of quantitative data regarding vapour content. The literature with reference to in-nozzle cavitating flows is scarce, since relevant research takes place in few facilities globally offering the high-end infrastructure required. Duke et al. [42] have performed X-ray radiography experiments in the Advanced Photon Source (APS) of Argonne National Laboratory (ANL) using a focused beam with a spot of 5×6 μm^2. A raster scanning method was implemented to cover the internal flow path of a 500 μm geometrically-constricted orifice. X-ray energies of 8 and 9 keV were used to irradiate a polyether ether ketone (PEEK) and a beryllium orifice of the same nominal internal geometry. The density distribution of the sheet cavity, which was verified to be prevailing in both cases, was obtained, while spectral analysis conducted in specific flow locations of the plastic orifice revealed the unsteady nature of the cavity trailing edge. Zhang et al. [43], also employing radiation generated at the APS synchrotron, investigated the dynamics of a quasi-stable sheet cavity arising in a two-dimensional, planar Venturi-type constriction. The test section having a width of 4 mm was bounded

by thin Plexiglas windows to minimise the X-ray absorption and allow for complementary high-speed imaging to be conducted. In addition, the flow was seeded with silver-coated particles to realise a novel X-ray-based PIV technique, offering information on the level of turbulence in the cavity region. Combined void fraction and shear-stress data showed that a weak yet relatively stable re-entrant flow motion was able to penetrate the entire cavity and cause oscillations in its topology.

Few studies performing XPCI with the use of synchrotron radiation have also been reported in the literature. The authors' group, Karathanassis et al. [44], using a 6 keV white beam at the APS, illustrated the dynamics of vortical (string) cavitation in an abruptly-constricting axisymmetric orifice with a minimum diameter of 1.5 mm. The visualisation took place at 67,890 fps with a spatial resolution of 5 μm/pixel and revealed that the fine-feature fluctuation of the vortical cavities is explicitly correlated with the magnitude of the underlying longitudinal vortices. In a follow-up experiment utilising a 12 keV white beam, the influence of viscoelasticity on cloud and string cavitation for the same flow layout was illustrated. Moon et al. [45] managed to obtain high-speed images at 67,890 fps of vortical cavitation in a steel fuel injector using XPCI. Nevertheless, the flow had to be seeded with tungsten particles to obtain enough contrast in the radiographs. Very recently, Tekawade et al. [46] carried out the first XPCI tomographic reconstruction of the two-phase flow setting in inside a steel injector at realistic operating conditions.

The overview of the relevant literature confirms that X-ray imaging techniques have evolved over the years, thus allowing the visualisation and quantification of complex two-phase flow fields. However, highly transient, wall-bounded cavitating flows at small length-scales with three-dimensional dynamic behaviour still pose great imaging challenges due to the high photon flux required to penetrate material, as well as the increased temporal and spatial resolution necessary for the faithful capturing of cavitation evolution. The present work constitutes, to the authors' knowledge, the first to provide time-resolved, qualitative XPCI and quantitative absorption-imaging data in a comparative manner with reference to an in-nozzle cavitating flow exhibiting distinct transient features, such as cavity shedding and vortical cavitation. The obtained experimental results shed light on the amount of information that can be extracted by each method regarding the extent of vapour content and cavity-cloud dynamics, as well as the fundamental flow processes designating the topology of the different cavitation regimes. The content of the manuscript is organised in four topics presented in the following paragraphs. X-ray beam characteristics and the experimental layout implemented are described in Section 2, while the post-processing methodology applied to extract physical information from the raw radiographs is discussed in Section 3. Qualitative and quantitative results produced by XPCI and absorption imaging are assessed in a comparative manner in Section 4 and the main findings of the investigation are outlined in Section 5.

2. Experimental setup

The experimental campaign leading to the results presented in this work was conducted at the APS in ANL. Sector 7 of the APS storage ring was operated at the hybrid pulsation cycle having an overall revolution time of 3.682 μs and comprising 9 pulses in total, as shown in **Fig. 1**. The pulsation sequence was adjusted through the X-ray chopper to 8 groups of septuplet pulses with a 51 ns gap in-between them, to allow enough signal to be acquired by the scintillator, while at the same time keeping blurring effects minimal. The 500ns-long train of pulses used, in essence designated the exposure time for the visualisation. A helical super-conducting undulator generated the X-ray beam with a photon flux approximately equal to 5.5×10^{15} photons/s/mm^2.The beam energy was selected equal to 11.88 keV, a value close to that giving the maximum contrast between liquid and vapour phases (approximately 10 keV [42]). At the same time, the photon energy is high enough to allow a percentage of the irradiation to penetrate through the nozzle material and liquid/vapour mixture, hence leading to measurable signal-to-noise ratio in the scintillator crystal.

Helical superconducting undulators offer great capability of beam-characteristics adjustment compared to other undulator technologies, in the sense that the emitted spectrum is dominated by the first harmonic. Moreover, the on-axis heat load is much smaller compared to that of a planar undulator

and allows to increase vastly the central-aperture photon flux. For the current study, the undulator was operated at a current of 120 A leading to spectrum first harmonic of 11.88 keV but also corresponding to an undulator (deflection) parameter K smaller than unity. For such a value of K, the peak flux of the second harmonic is an order of magnitude smaller compared to that of the first, while higher harmonics are eradicated. Hence, the beam spectrum approaches the nature of a high-flux 'pink' beam and, therefore, beam hardening effects are alleviated [47]. A 'pink' beam differs from a monochromatic beam, in the sense that its bandwidth is tuned by the selective reflection of photons from a coated X-ray mirror at grazing angles, rather than the use of a monochromator, with the resulting flux being orders of magnitude higher.

A 10 mm in diameter scintillator crystal (LuAg:Ce) with a thickness of 0.1 mm received the attenuated X-ray beam after its interaction with the investigated test-section and converted it to visible light, subsequently captured by a high-speed camera (Photron SA-Z) at 67,890 fps. The scintillator was placed at a relatively large distance of 350 mm from the test piece for the XPCI campaign to be able to account for the contribution of refracted X-rays to the measurable signal. On the contrary, for the absorption imaging the relative distance was 80 mm, the minimum allowed by the physical layout of the examined system, to ensure that the signal was absorption dominated. In an effort to increase the spatial resolution, the X-ray beam was collimated to a field of view of 2.56×2.56 mm, discretised by 512×512 pixels, and, thus, resulting to a resolution of 5 μm/pixel. As the orifice length (5 mm) was larger than the selected field of view, it was segmented into five overlapping panels and each panel was irradiated successively, in a similar manner to the authors' previous works [50,54], as illustrated by the inset of **Fig. 1**. Besides, as also emphasised in previous works, the fine scanning along the orifice length was also dictated by the spot shape of the X-ray beam, which was collimated to a circular cross-section and hence the photon flux at the edges of the square active window was somewhat reduced compared to the inner-spot region.

The geometrical layout of the orifice under investigation is also shown in **Fig. 1**. The fixed metallic needle constricting the flow, along with the offset of the 1.5mm in diameter nozzle from the symmetry axis of the upstream (sac) volume promote the onset of an asymmetrical cavitation topology, resembling the two-phase field commonly prevailing in fuel-injection equipment. A more detailed discussion on the orifice design can be found in [44]. It should be noted that an organic polymer (PolyEther Ether Ketone-PEEK) was preferred as the orifice material for the present series of experiments, whereas a carbon-fibre composite was selected in previous works of the authors referring to XPCI [44,48]. It was verified by prior experiments employing a carbon-fibre piece that the signal-to-noise ratio for absorption imaging was too low to extract meaningful data. Despite the low atomic number of carbon, the carbon-fibre layering process required to realise the internal-flow path dictated the use of an adhesive resin to bond the overlapping carbon-fibre sheets and was the culprit for the extensive beam attenuation. Besides, carbon-fibre layering onto a metallic mould did not allow the accurate control of the orifice entrance curvature. **Fig. 2** depicts raw radiographies obtained for both test pieces. As can be seen on the left panel of the figure, the entrance curvature is quite asymmetrical for the carbon-fibre piece, whereas a much more uniform curvature profile is evident for the PEEK one. Although PEEK durability is lower compared to carbon fibre, the safety factor was still acceptable for the new test-piece regarding the examined pressure range. The nozzle geometry was verified not to deform during experiments. More specifically, its cross-sectional outline along the line-of-sight obtained through raw radiographs with imposed flow was overlaid against the respective obtained by preliminary radiographs with stagnant liquid and demonstrated to be identical. Besides, the orifice diameter was measured at 12 locations equally spaced along its length and the resulting average value was 1.474 ± 0.007 mm, which is within machining tolerances.

Since the investigation is primarily relevant to fuel-injection equipment, the working medium was diesel fuel circulating in the hydraulic flow loop at a nominally steady flow rate. The prevailing flow conditions within the nozzle for the test cases examined were characterised with the use of the Reynolds and Cavitation numbers. Their definition and examined range are reported in **Table 1**. Through an active cooling system, the fuel was kept at a temperature of 313.0 ± 1.0 K, constantly monitored through type-K thermocouples inserted at the inlet/outlet manifolds. An axial-turbine flow

meter was used to measure flow rate, while the injection and back-pressures were recorded by transducers also mounted at the inlet/outlet manifolds. A total of 10 test cases were examined, as summarized in **Table 1,** accounting for both XPCI and absorption measurements. It should be noted that two values of the needle-lift were considered (0.5 mm and 1.0 mm), since they promote different cavitation regimes, as will be demonstrated in the results section. Furthermore, measurable signal was obtained only for XPCI in the case characterised by CN=2.0; the specific case was therefore omitted from the absorption measurements.

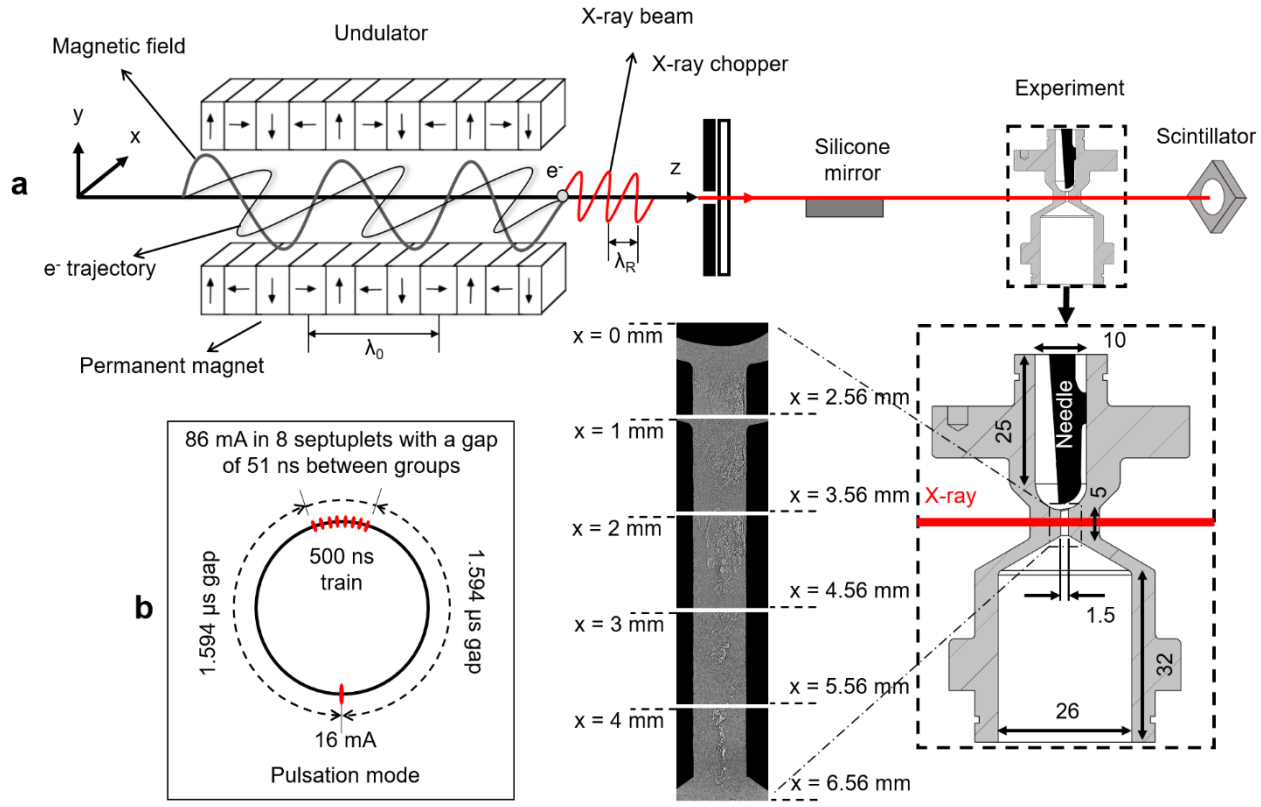

Fig. 1 (a) Schematic of the experimental setup for the X-ray imaging and (b) beam-pulsation mode. The spatial period of the undulator magnets λ_0 is equal to 31.5 mm, while the characteristic wavelength λ_R corresponding to the X-ray energy of 11.88 keV is 0.104 nm. A detailed view of the test-piece with basic dimensions is also shown, along with a sample series of XPCI radiographs illustrating the five distinct irradiation locations. The radiographs correspond to a top view of the flow field and the flow is front top to bottom, with the hemispherical needle tip being discernible at X=0 mm. The X-ray setup is not to scale and the dimensions of the model are in mm.

Table 1 Matrix of the flow conditions examined. The Reynolds number has been defined as $Re = u \cdot d/\nu_{fuel}$, where the nominal velocity u has been calculated thought the imposed flow rate and d (=1.5 mm) is the orifice diameter. The cavitation number has been defined as $CN = (p_{inj} - p_{back})/(p_{back} - p_{sat})$. Values for the fuel viscosity ν_{fuel} and saturation pressure p_{sat} have been obtained by [49].

Case No.	X-ray technique	Needle lift [mm]	CN	Re	p_{inj} ×10^5 [Pa]	p_{back} ×10^5 [Pa]	T_{fuel} [K]
1	Absorption	0.5	4.0	35500	27.3	5.6	312.4
2			6.0		26.4	3.9	313.4
3		1.0	4.0		27.6	5.7	312.5
4			6.0		26.9	4.0	312.9
5	XPCI	0.5	2.0	35500	35.0	11.8	313.3
6			4.0		28.7	5.9	314.0
7			6.0		28.1	4.2	313.0
8		1.0	2.0		34.1	11.4	313.0
9			4.0		27.7	5.7	313.0
10			6.0		25.6	3.8	314.0

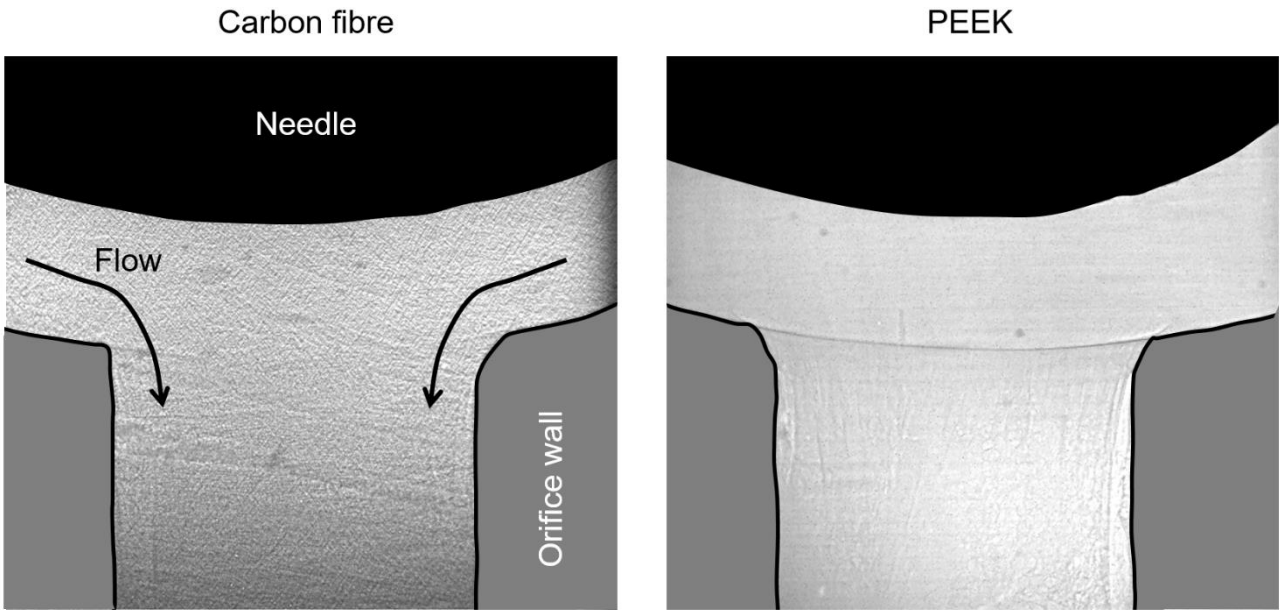

Fig. 2 Raw radiographs illustrating the differences in the geometrical layout of the orifice-entrance region between the current PEEK model and the carbon-fibre one used in previous investigations [44,48].

3. X-ray radiographs processing

3.1 XPCI image processing

A set of 10,000 12-bit greyscale radiographs were acquired per irradiated location to enhance the accuracy of the statistical assessment of the XPCI data. In order to detect the liquid/vapour interface, a series of post-processing techniques were applied in a sequential manner. The overall methodology is similar to that adopted in [44] and it is only briefly outlined here (**Fig. 3a**). As a first step to enhance contrast, each examined image was subtracted from a background image obtained with stagnant liquid in the orifice. The phase congruency method [50] was subsequently applied to detect the edges that define the outline of the vaporous structures. The basic principle of the method states that the frequency (Fourier) components of important, edge-like features in an image have the same phase. Phase congruency is maximised for salient features and since it constitutes a non-dimensional quantity defined in the Fourier domain, its magnitude is not affected by variations in image brightness or contrast. Identified features were dilated and smoothened, using a Gaussian filter, to form the outer extent of the cavities. Finally, an adaptive thresholding technique [51] was applied to binarise the images. Small, unconnected objects (impulse noise, refer to the respective panel of **Fig. 3a**) with areas below 10 pixels were removed from the final image.

3.2 X-ray absorption image processing

The presence of vapour in the beam path leads to an increase of the percentage of irradiation I' reaching the scintillator compared to the respective I for the case where the nozzle is filled by liquid. Postulating that beam attenuation occurs only due to absorption in the irradiated material layers, the projected (line-of-sight) accumulated vapour thickness can be calculated through the Beer-Lambert law:

$$I'/_I = \quad e^{-\mu \cdot \lambda} \tag{1}$$

where μ is the attenuation coefficient of the liquid medium (the respective of vapour corresponds to negligibly small values) and λ is the vapour mean path (thickness). The narrow-spectrum beam produced by the helical super-conducting undulator along with the minimisation of the sample-to-detector distance render valid the use of the exponential-decay law to produce quantitative data regarding the in-nozzle vapour content. In addition, **Eq. (1)** infers that the original X-ray intensity is influenced only by the sample material layers and their relevant thicknesses. Nevertheless, X-rays behave as electromagnetic waves and therefore refraction occurs in the interfaces of media with different densities. The refractive index is expressed as a complex number $n = 1 - \delta + i\beta$ with reference to X-rays, where δ is of the order of 10^{-5} in solids and about 10^{-8} in air and the imaginary part β obtains even smaller values [52]. Hence, the X-ray refractive index obtains near-unity values, indicating the weak interaction with matter. The real part δ of the index represents the shift in the irradiation-wave phase, while the imaginary part β the attenuation in the wave amplitude [53]. As the X-ray wave interacts with matter, both mechanisms contribute to brightness gradients evident on the obtained radiographs. Therefore, a certain level of 'phase-contrast' contamination exists in the absorption images, which is though minimised as the scintillator location approaches the sample and the majority of diverging rays do not impinge on the crystal. Contrast due to phase shift appears as fringes in the transmission distribution at the location of an interface.

5,000 images were recorded at each panel of the test sample during the absorption-imaging campaign. A smaller number of raw-images compared to XPCI was deemed as sufficient to extract quantitative information regarding the vapour extent, as the capturing of fine interfacial fluctuations is not within the scope of the specific imaging layout. Transmission plots were correlated to the ensemble vapour path designating the brightness value of each pixel within the images using **Eq. (1)** and the attenuation coefficient determined through a calibration method discussed in the next paragraph. Beam transmission was calculated by dividing each examined image by a 'background' corresponding to pure liquid within the orifice (**Fig. 3b**). To mitigate the influence of any fringes stemming from phase shift on the absorption data, transmission plots were smoothened by averaging the brightness of ten successive pixels in a row, as shown in the second panel of **Fig. 3b**. The resulting image (third panel of **Fig. 3b**), although it cannot capture fine interfacial features in the same manner as XPCI, elucidates the in-nozzle vapour content. It should be noted that since a line-of-sight method is employed, the exact location of the vapour phase is not specified in the three-dimensional space like in tomographic reconstruction but rather the projected vapour path is measured with high temporal and spatial resolutions. Furthermore, the distribution of the local chord length of the nozzle cross-section is also given in **Fig. 3b**, which can be used to normalise the vapour-path values to produce the line-of-sight integrated vapour fraction. Vapour-fraction values are straightforward and have been reported for two-dimensional flows [37,38], yet do not have a clear physical meaning with reference to axisymmetric flows exhibiting extensive three-dimensional features. In such cases, the line of sight is highly plausible to pass through a number of vapours structures overlapping with liquid regions. Hence, the vapour fraction value would constitute a 'lumped' quantity encompassing all structures. For this reason, it has been deemed as more suitable to express the in-nozzle vapour content in terms of overall path length, a practice that has also been adopted in relevant investigations [42,54,55].

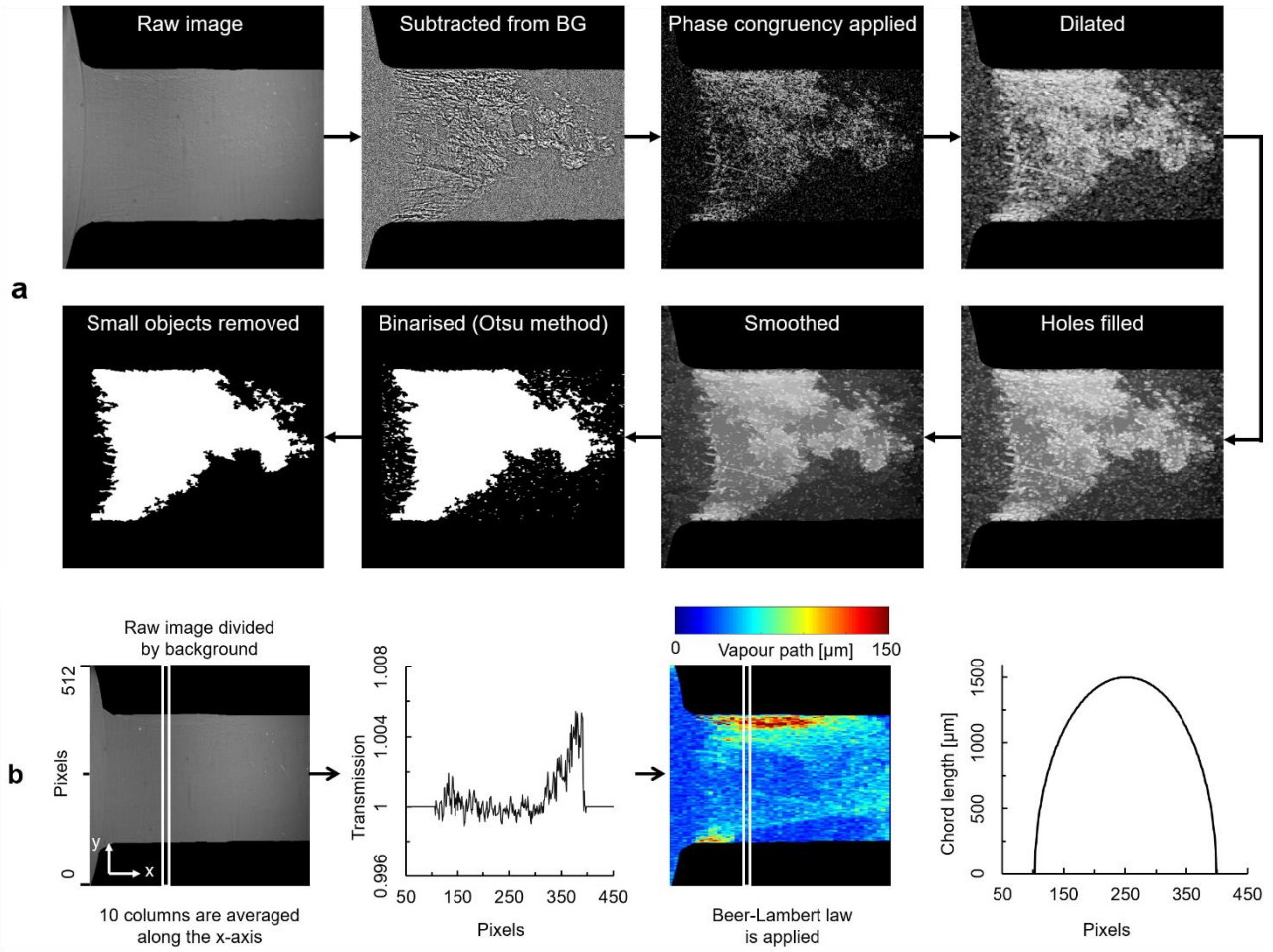

Fig. 3 Outline of the post-processing techniques employed to derive quantitative information from (a) the XPCI and (b) absorption raw radiographs. Two indicative time instances, corresponding to lift = 0.5mm, CN=4.0 for (a) and lift=0.5, CN=6.0 for (b), have been selected to illustrate the post-processing steps. The distribution of the local chord length c is also depicted on the right-hand side of (b) and can be used to convert vapour path λ values to vapour fraction a, as $a=\lambda/c$.

The value of the attenuation coefficient μ was determined through preliminary measurements, where droplets of the fuel sample were irradiated, in order to fit normalised transmission data to **Eq. (1)**. A fuel droplet expelled at the tip of a syringe placed in a cuvette was irradiated, as shown in **Fig. 4a**. Considering that the droplet retains an almost axisymmetric shape due to surface tension, liquid thickness can be directly measured by the obtained radiographs. The absorption coefficient is therefore determined by fitting an exponential-decay correlation to the section of the transmission curve corresponding to the fuel thickness, as annotated in **Fig. 4b**. It is also interesting to notice the fringes in the transmission distribution at the locations corresponding to interfaces between media with different densities and to the cuvette wall, highlighting the influence of phase-shift on the absorption data. The attenuation coefficient for the current setup was measured equal to $5.268 \cdot 10^{-5}$ μm^{-1}. This value was assigned to the coefficient μ of **Eq. (1)** to derive vapour-thickness data in the nozzle-flow experiments, with the beam transmission being calibrated against the background intensity I_{BG} for an orifice filled with liquid, as described in the previous paragraph.

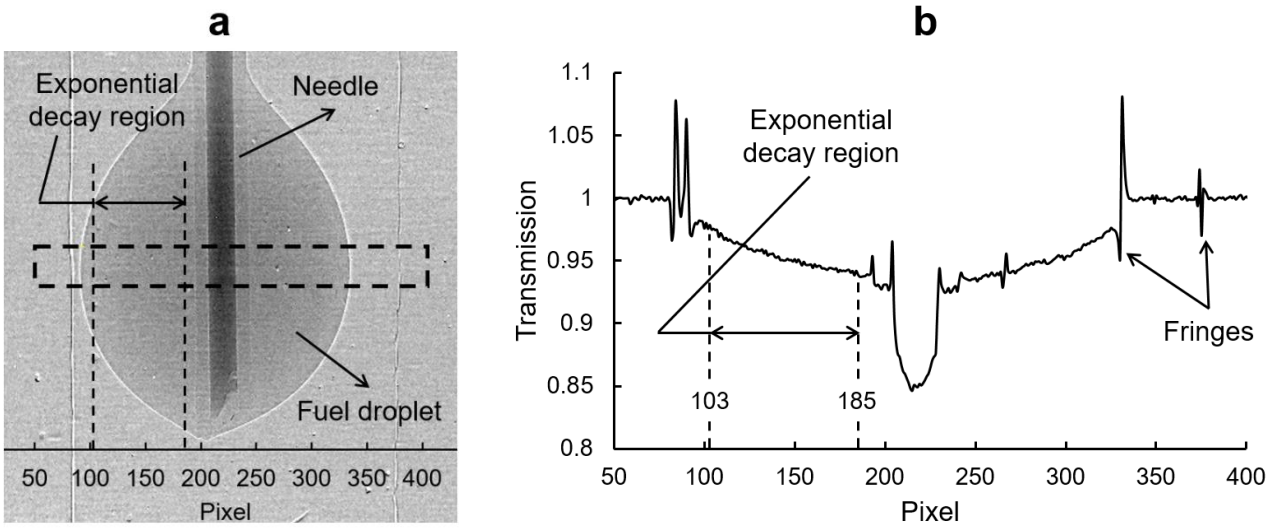

Fig. 4 Calibration process for the determination of the attenuation coefficient: (a) radiograph corresponding to the calibration test and (b) X-ray transmission distribution along the lateral dimension.

3.3 Experimental uncertainty

A standard error propagation analysis, as outlined in [56] has been applied to assess the uncertainties in the physical quantities calculated based on raw experimental data. The maximum experimental uncertainty associated with the Reynolds and Cavitation numbers were calculated based on the accuracy of instrumentation and geometrical uncertainties and found to be of the order of 3.1% and 1.7% respectively. The statistical uncertainty *U* associated with the qualitative XPCI data essentially refers to the uncertainty in the mean values of vapour-presence probability and standard deviation reported, which can be expressed as follows:

$$U_{\bar{a}} = \frac{\sigma_a}{\sqrt{n}},\ U_{\sigma_\alpha} = \frac{\sigma_a}{\sqrt{2(n-1)}} \tag{2}$$

where σ is the standard deviation of the measured probability a and n is the sampling population, i.e. the recorded frames in the current experiments. Owing to the significant number of images acquired, the average statistical uncertainties associated with the mean vapour-presence probability and respective standard deviation of a pixel value throughout all the irradiated panels, were found to be equal to 0.18% and 0.13%, respectively.

With reference to the absorption data, the uncertainty associated with the instantaneous vapour-path values U_λ is determined by the propagation of uncertainties in the values of primary measured quantities, namely transmission T and attenuation coefficient, as re-arrangement of **Eq. (1)**, leads to:

$$\lambda = \frac{\ln(T)}{\mu} \tag{3}$$

where the transmission T is actually a calculated quantity based on the attenuation induced on the beam of initial intensity I_0 in the cases where pure liquid and a two-phase mixture occupy the orifice:

$$T = \frac{I_1}{I_{BG}} = \frac{{I_1}/{I_0}}{{I_{BG}}/{I_0}} \tag{4}$$

where I_1 and I_{BG} are the intensities of transmitted beam in the presence and absence of vapour, respectively, while I_0 is the intensity of the X-rays produced by the storage ring. Therefore, applying partial-derivative error propagation to **Eq. (3)**, the relative uncertainty in the instantaneous vapour-path λ is given by:

$$\frac{U_\lambda}{\lambda} = \sqrt{\left(\frac{U_{ln\mathrm{T}}}{\ln T}\right)^2 + \left(\frac{U_\mu}{\mu}\right)^2} = \sqrt{\left(\frac{U_T}{T}\right)^2 \cdot \left(ln(T)\right)^{-2} + \left(\frac{U_\mu}{\mu}\right)^2} \tag{5}$$

The uncertainty in transmission is specified through **Eq. (4)**, as follows:

$$\frac{U_T}{T} = \sqrt{\left(\frac{U_{\left(\frac{I_1}{I_0}\right)}}{{I_1}/{I_0}}\right)^2 + \left(\frac{U_{\left(\frac{I_{BG}}{I_0}\right)}}{{I_{BG}}/{I_0}}\right)^2} \tag{6}$$

Combining with **Eq. (6), Eq. (5)** can be re-arranged as:

$$\frac{U_\lambda}{\lambda} = \left\{\left[\left(\frac{U_{\left(\frac{I_1}{I_0}\right)}}{{I_1}/{I_0}}\right)^2 + \left(\frac{U_{\left(\frac{I_{BG}}{I_0}\right)}}{{I_{BG}}/{I_0}}\right)^2\right].\left(ln(T)\right)^{-2} + \left(\frac{\varepsilon_\mu}{\mu}\right)^2\right\}^{1/2} \tag{7}$$

The experimental uncertainty in transmissions I_1/I_0 and I_{BG}/I_0 was assumed equal and estimated of the order of 0.3% considering the deviation of the transmission values measured during the calibration process (refer to **Fig. 4b**) from the theoretically predicted ones by **Eq. (1)**. Besides, the uncertainty in the attenuation coefficient μ can be derived in a similar manner to that of the vapour path λ, since $\mu = \ln\left(\frac{I_{drop}}{I_0}\right)/d$, where I_{drop} is the attenuated beam intensity due to absorption by the fuel droplet and d is the droplet diameter in the calibration test. The error in d stems only from the visualisation spatial resolution and is equal to 0.4%, leading to an overall uncertainty for μ equal to 4.2%. As the transmission values lie in the range 1-1.08, the average uncertainty in the instantaneous λ values was found to be 7.3%. The respective uncertainty in temporally-averaged values also contains the contribution of statistical uncertainty, **Eq. (2)**, as follows:

$$U_{\bar{\lambda}} = \sqrt{U_\lambda^2 + U_{\bar{x}}^2} \tag{8}$$

Once again, due to the significant number of images recorded, the contribution of statistical uncertainty is almost negligible and the average uncertainty in $\bar{\lambda}$ values amounts to 7.4%.

4. Results

4.1 Time-resolved cavitation morphology

As discussed earlier, the processed results of the XPCI experiment depict a planar projection of vapour/liquid interfaces arising within the orifice, as an outcome of the difference in the refractive index of diesel in liquid and gaseous forms. As demonstrated in **Fig. 5**, the temporal evolution of cavitation topology can be illustrated by processing and analysing consecutive radiographs at all locations (for brevity only the entrance and exit of the orifice have been illustrated). **Fig. 5a** depicts the cavitation topology at the orifice inlet for the low needle lift examined (L=0.5mm) and well-established cavitation (CN=4.0). A clearly discernible, three-dimensional cloud cavity sets in, having a stable core yet an unsteady closure region. On the contrary, **Fig. 5b** depicts a longitudinal vortical cavity propagating all the way to the orifice outlet. As can be seen, its topology is highly perturbed with a multitude of small features, which can be clearly captured due to the high spatial and temporal resolutions of the employed technique.

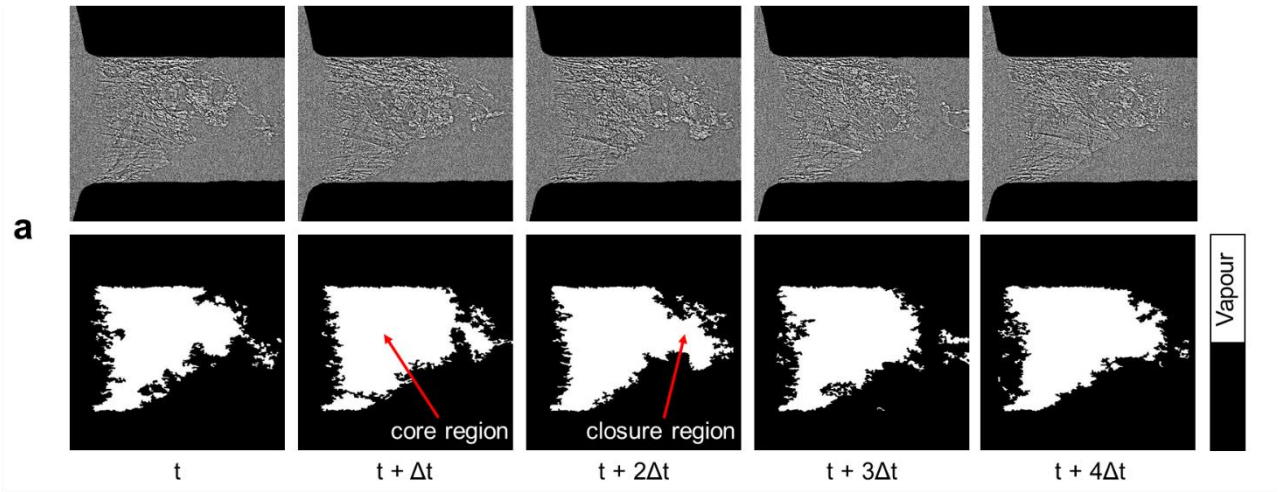

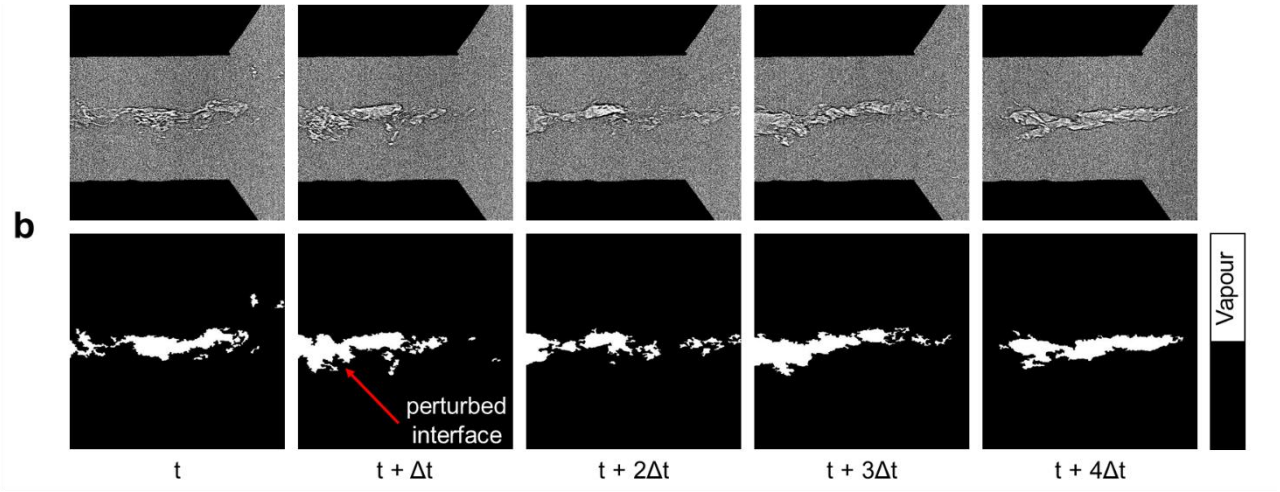

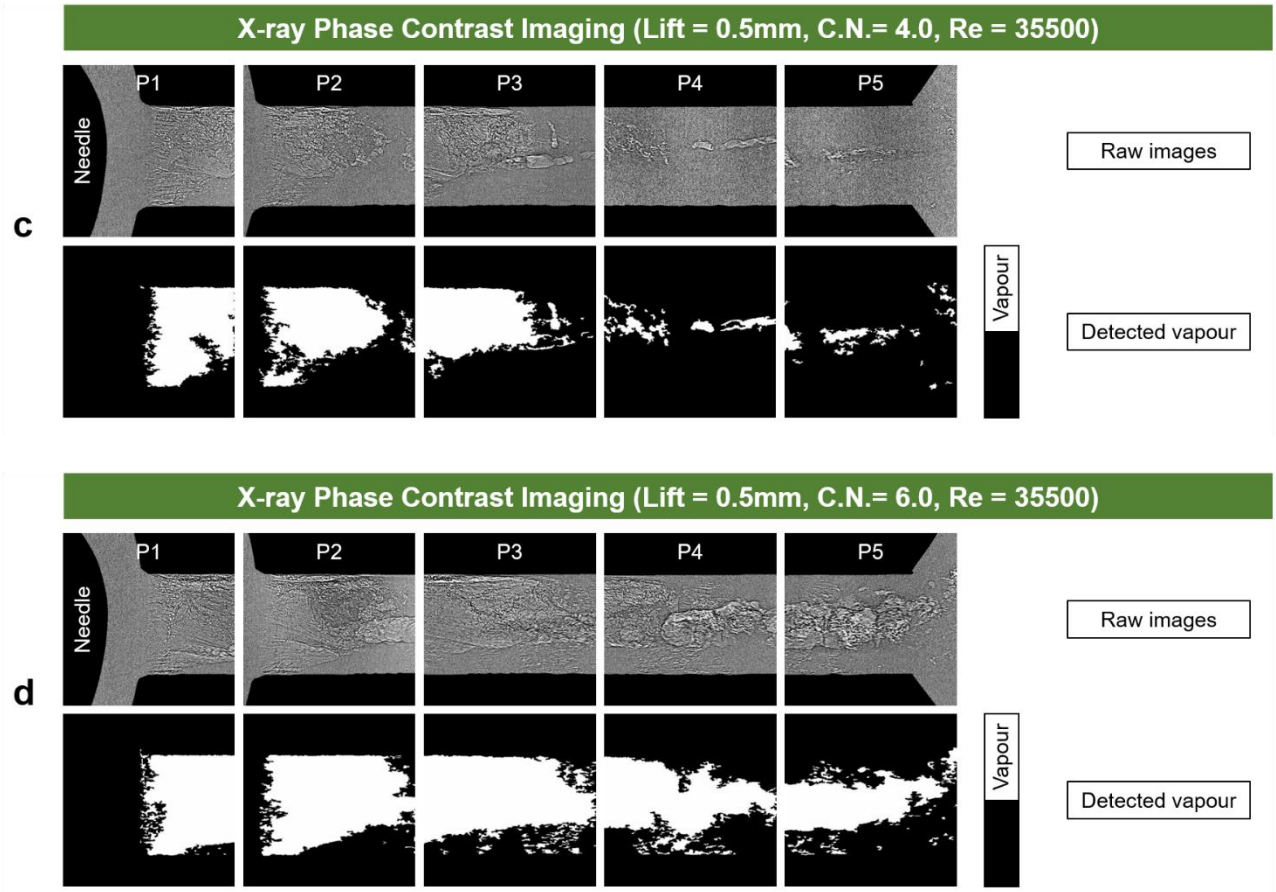

Fig. 5 Temporal evolution of cavitation topology derived through XPCI: (a) L=0.5, CN=4.0, panel P2 (orifice inlet) and (b) L=0.5, CN=4.0, panel P5 (orifice outlet). Animations for all panels are offered in supplementary movies for (c) L=0.5, CN=4.0 (Multimedia view) and (d) L=0.5, CN=6.0 (Multimedia view). Raw and post processed images are depicted on the upper and lower panels of each figure. Δt is the time period between successive frames, equal to 1.473×10^{-5} s.

As already mentioned, in order to fully elucidate the morphology of the flow-field evolution and verify any repetitive behaviour in its nature, a set of 10,000 radiographs were acquired at each location for all examined conditions. All processed images were then used to calculate the mean probability of vapour presence and its standard deviation. **Fig. 6a** depicts the averaged flow field within the orifice and illustrates that a relatively stable cloud cavity (high probability values) sets in throughout the nozzle circumference for CN=4.0 and 6.0, regardless of the needle lift. On the contrary, for the low CN (=2.0) value, scarce cavitation develops at the orifice entrance as indicated by the low mean (**Fig. 6a**) and high standard deviation values (**Fig. 6b**). It must be pointed out that the cloud topology is asymmetrical, which should be attributed to a three-dimensional separation at the contraction region. This pattern should be expected due to the high value of the Reynolds number, the wall curvature of the chamber preceding the nozzle, which can trigger flow instabilities (e.g. of the Goertler type) and the asymmetrical inlet velocity profile (refer also to **Fig. 1c**). Moreover, the standard deviation contour plots (**Fig. 6b**), make evident that an increase in cavitation number increases the length of the mentioned attached cavities, a common behaviour for the low and high-needle lift cases.

At a next step, the effect of needle lift on the cavitation topology was assessed, which can be highlighted by comparing the cases corresponding to lift of 0.5mm and 1.0mm for CN=4.0. For L=0.5, a longitudinal vortical cavity appears to extend to the orifice outlet. On the contrary, for L=1.0 the entire cavity trailing edge is wider and a cloud shedding process is also indicated by the high standard-deviation values. The standard deviation images also highlight the elongated vortical structure, which is present at a high fluctuating form for CN=4.0 but barely evident for CN=2.0. The presence of longitudinal cavitating vortices prevailing in the orifice is owed to vortex roll-up in the

sac region, facilitated by the high-blockage ratio for low needle lifts, as has been identified in previous studies [44,48]. As CN increases the cloud and vortical cavities become more extensive and intertwine, hence it becomes challenging to differentiate between them.

A flow feature that is also worth mentioning, can be discerned at P3-P5 of high CN cases, where slender cavitation structures attached to the orifice wall emerge, elongate and are eventually entrained toward the main cloud core. Onset of these cavitation structures is the result of machining imperfections in the orifice diameter, which were also noticeable in the raw images as illustrated in **Fig. 6c.** Albeit, in essence, these are unwanted features that somewhat obscure the cavitation regimes, they demonstrate the enhanced resolution of the employed XPCI setup.

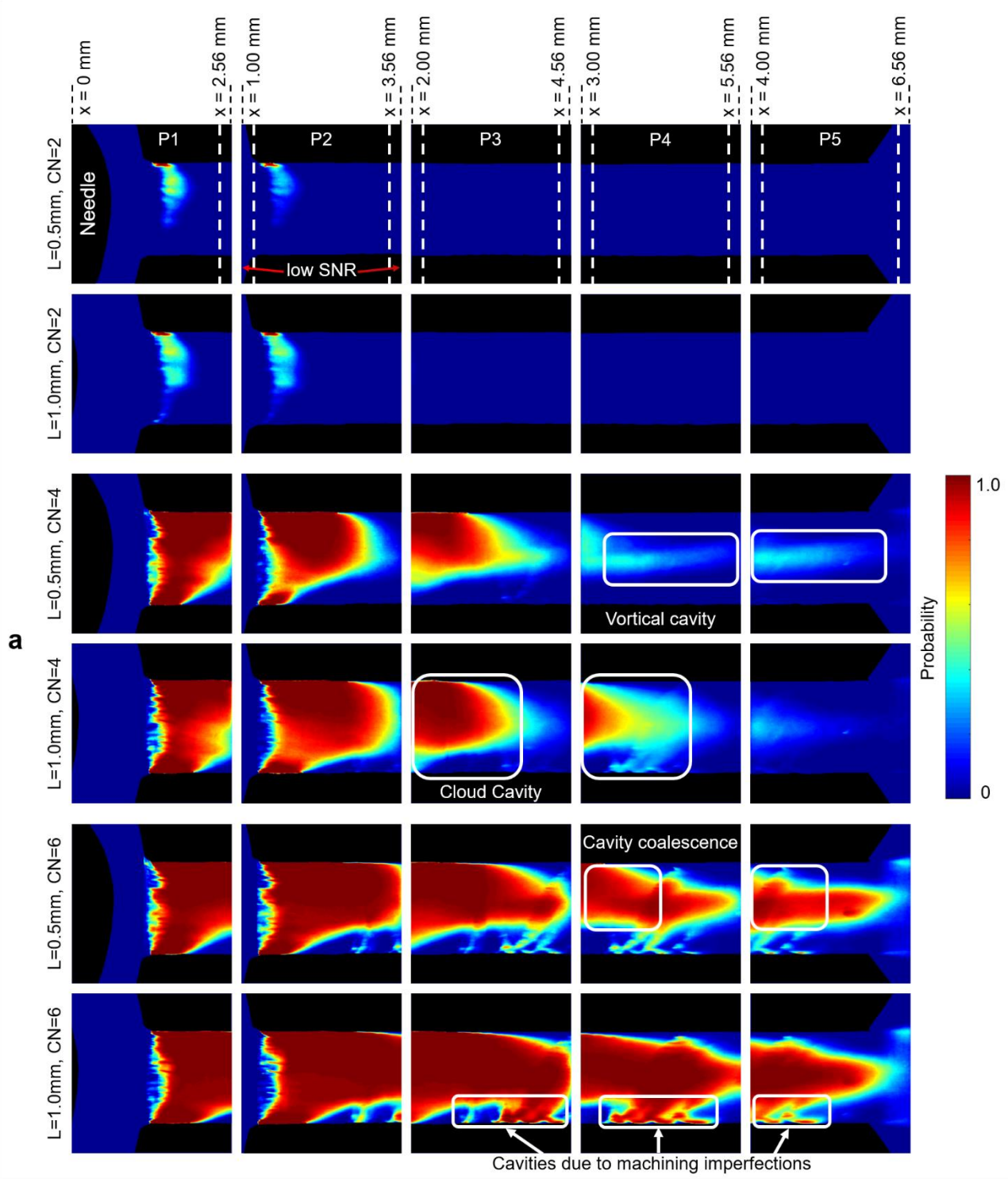

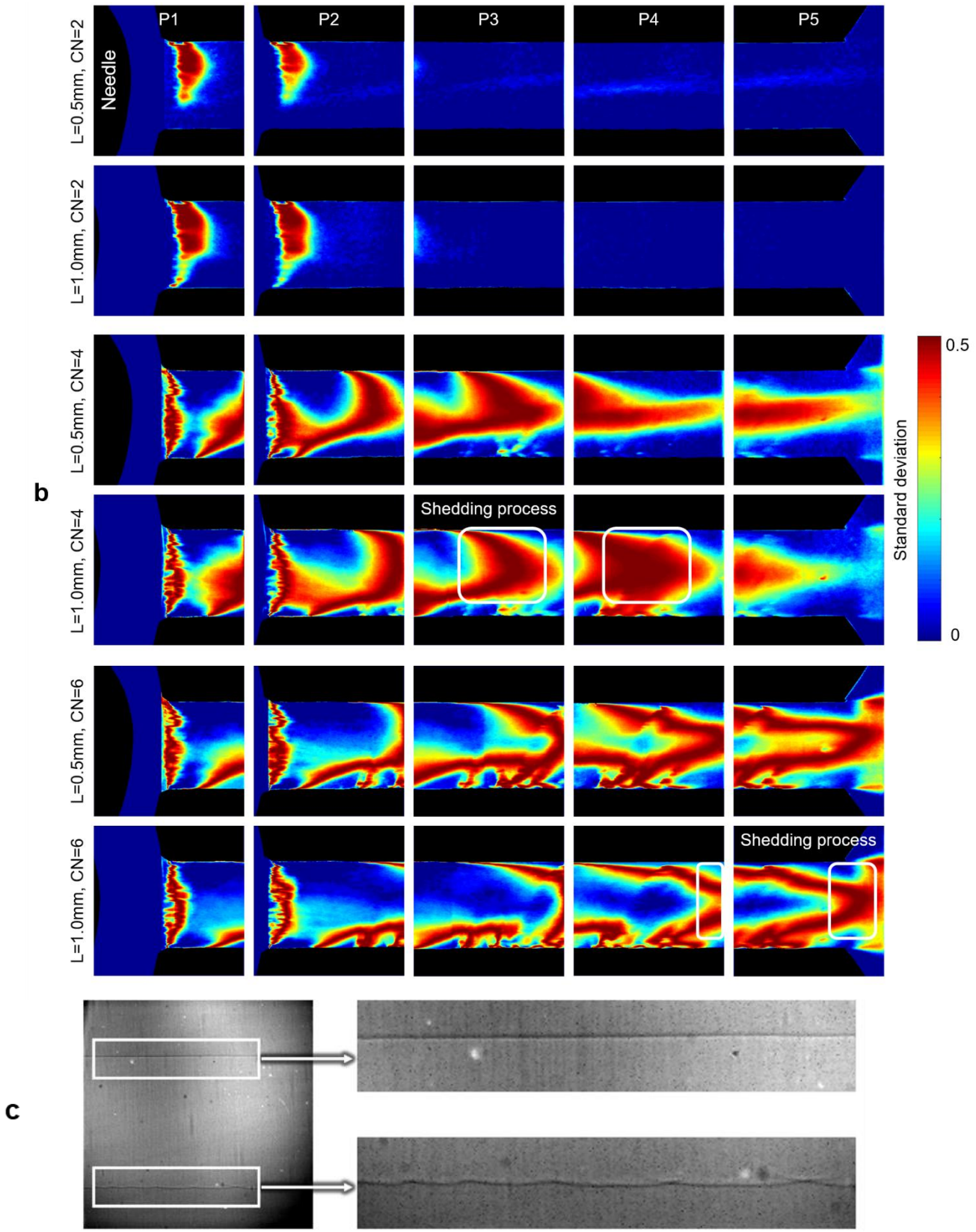

Fig. 6 Contour plots of (a) the time-averaged vapour-presence probability and (b) respective standard deviation for different flow conditions. Flow is from left to right and distinct flow features have been annotated in each panel. Dashed white lines in the vicinity of panel edges indicate regions (~0.2mm wide) of reduced signal-to-noise ratio (SNR). (c) A raw radiograph of the fourth characteristic region (P4) depicting machining imperfections in the projected bottom side of the orifice wall.

A quantitative comparison of the examined cases is available in **Fig. 7** depicting the spatially-averaged vapour-presence probability (**Fig. 7a**) and standard deviation (**Fig. 7b**) in each characteristic irradiated location. The rationale is to provide an overall metric of the vapour extent within the orifice, as indicated by the XPCI data, since the positions of irradiated panels are explicitly correlated with the axial co-ordinate running through the orifice length in the manner shown in **Fig 7c**. **Fig. 7a** illustrates that the presence probability tends to decrease as the flow travels towards the nozzle outlet, i.e. from P1 to P5, in all cases. There is an exception in P3 of the case characterised by L=1.0 and CN=6.0, where a maximum in the probability distribution is evident. This is due to the additional presence of slender cavities arising from machining imperfections, as described earlier. Moreover, increasing the cavitation number results in higher probability of vapour presence in all characteristic regions. The effect of needle lift can also be clearly deduced, as lower lift results in smaller cloud cavities and reduced vapour probabilities. It is worth mentioning that in P5 for the CN=4.0 case, although the cloud cavity is not present, the longitudinal vortex cavity sets in for low needle lift and results in a larger mean probability value compared to that for high lift. Additionally, the standard deviation plots for CN=6.0 (**Fig. 7b**) reveal a positive slope, owing to the increase in the fluctuations of cavities in flow regions closer to the nozzle exit, as the coherence of the invariable cloud core is disrupted. On the other hand, for CN=4.0, it is noticeable that the standard-deviation distribution obtains an opposite slope, as we move further downstream the orifice entrance, indicative of the decaying coherence of all vaporous structures. Moreover, the highest measured standard-deviation occurs at P4 for the case characterised by lift of 1.0 mm and CN=4.0, which suggests a highly unsteady cavity trailing edge indicative of a shedding behaviour.

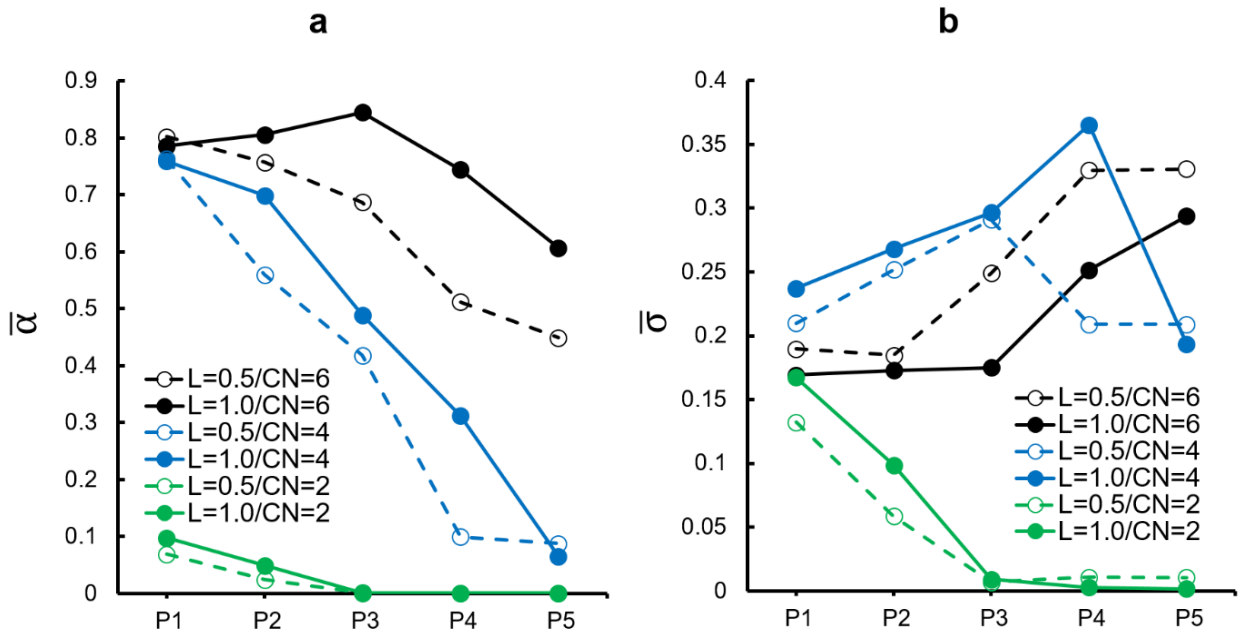

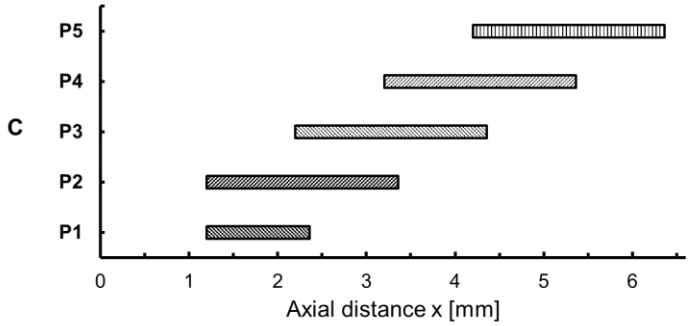

Fig. 7 Temporally- and spatially-averaged values of (a) vapour-presence probability $\bar{\alpha}$, and (b) standard deviation $\bar{\sigma}$, along the irradiation panels. Graphs values have been calculated by spatially averaging the range of probability and standard-deviation values obtained in each characteristic location (irradiation panel P) excluding low signal-to-noise regions, refer to the mean and standard-deviation contour plots of **Figs. 6a-b**). (c) Position of each irradiation panel with reference to the axial co-ordinate. Geometrical constriction occurs at x=1.0 mm, refer to the schematic of **Fig. 1a**.

The instantaneous evolution of cavitation topology, depicted in **Fig. 5** made evident a plethora of transient features with reference to both cloud and vortical-cavitation regimes. In order to further assess the XPCI capability of capturing rapid cavity dynamics, the potential periodicity of transient features has been examined, so that correlations with fundamental flow processes can be made. Initially, the temporal evolution of the cavity length was recorded for the cloud cavitation regime (lift of 1.0 mm) and a Fast Fourier Transform (FFT) analysis was applied to verify the presence of a periodical shedding cycle. The control windows selected to detect cloud break up, i.e. length variation, were determined based on the averaged vapour-presence probability plots. In other words, it was verified that the region of expected break-up was bound by an upstream vapour region ($\overline{\alpha}$ approaching 1) and a downstream liquid region ($\overline{\alpha}$ approaching 0). Besides, during the post-processing of the radiographs, it was verified that the cloud length in the specified panels was never detected to be equal either to zero or to the panel dimension.

Fig. 8 depicts the frequency spectrum of the cavity-length waveform for the test cases exhibiting a well-established cloud cavity (CN≥4.0). Clear dominant frequencies can be discerned for both cases characterised by CN=4.0 (**Fig. 8a**) and CN=6.0 (**Fig. 8b**), with the respective values being equal 5,114 and 5,725 Hz. It should be noted that the image acquisition frequency is more than ten times higher compared to the peak frequencies detected. Hence, the sampling rate is in compliance with the Nyquist condition and sufficient to capture the periodicity of the examined flow process. The presence of frequency peaks is indicative of a shedding cycle from the cavity trailing edge with corresponding Strouhal numbers ($St=f \cdot L_c/u$) equal to 0.23 and 0.39, respectively. It must be noted that the cavity length was used as the characteristic length L_c for the definition of the Strouhal number, as suggested by Franc and Michel [57], while the flow velocity u was determined through the imposed flow rate. Sato and Saito [58] have performed optical imaging in axisymmetric orifices with length-to-diameter ratios in the range ~2-5 for cavitation regimes spanning from incipient to super-cavitation occupying the entire orifice length. The re-entrant jet mechanism was found to govern the cavity shedding in their experiments and the measured Strouhal numbers lied in the range of 0.29-0.37 for well-established cavitation, depending on the cavitation number. Given that the reported St values are in agreement with the current observations and that shedding occurs only from the cavity closure region for the examined flow conditions, XPCI data suggest that re-entrant jet motion persists in the region and designates the dynamics of the shedding sequence.

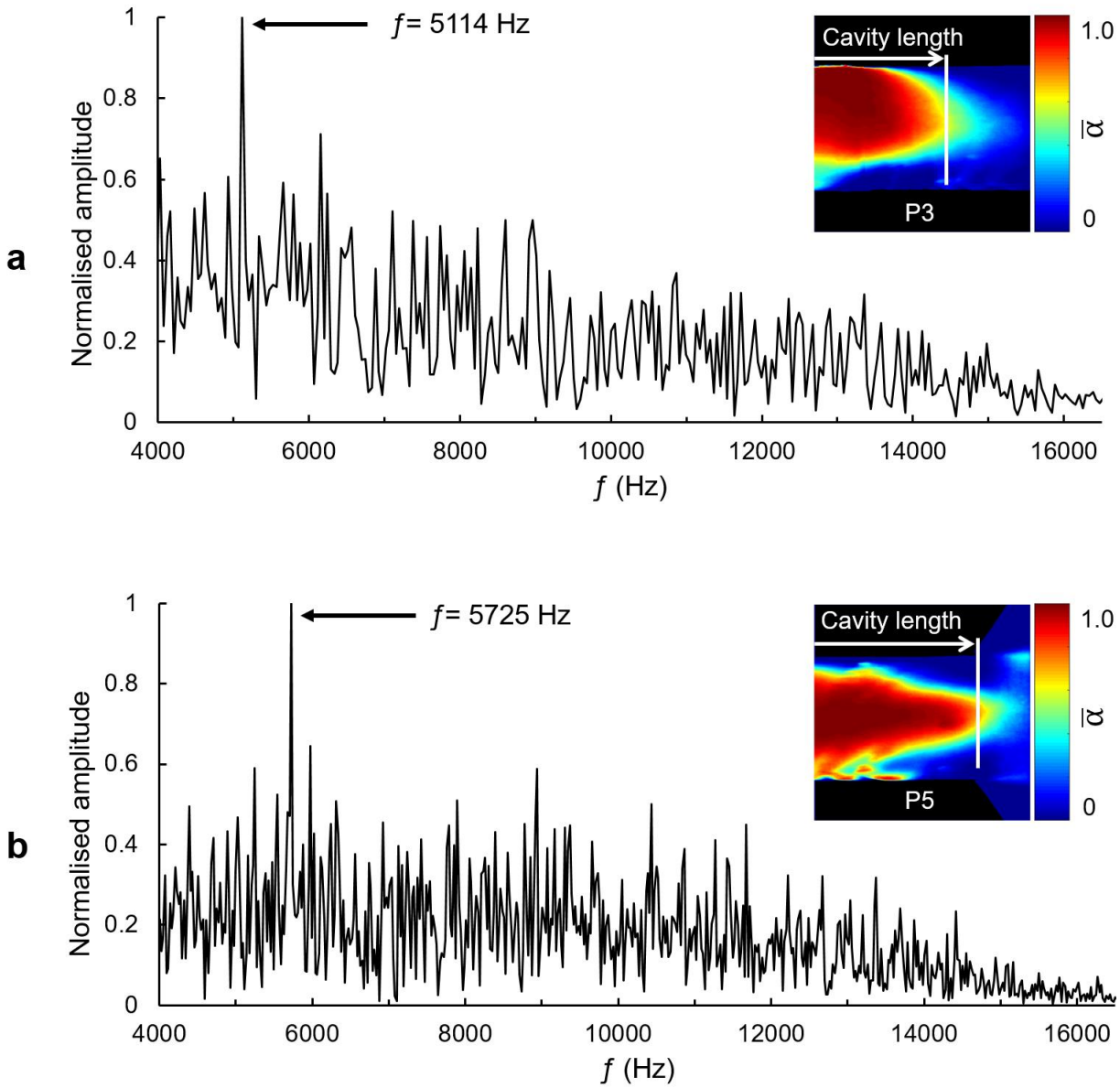

Fig. 8 Illustration of cloud cavity dynamics for needle lift of 1mm: Frequency spectrum for cavity shedding obtained through FFT: (a) CN=4.0, (b) CN=6.0. The cloud cavity breakup is identified when the cloud width gets below a defined threshold and subsequently the cloud length is measured.

XPCI can also provide insight on the dynamics of vortical cavitation, as also shown by the authors in [44]. It has been theoretically proven that the radius of a vortical cavity stemming from a longitudinal vortex of constant recirculation intensity Γ obtains a maximum value and oscillates around that with a frequency f that scales with Γ, i.e. $\Gamma \sim f \cdot 4\pi^2 \cdot r_c^2$, where r_c is the cavity radius [32,57,59]. Hence, capturing of the elongated-cavity interfacial fluctuations provides information on the underlying vortical flow field, at least in a relative manner. As illustrated in **Fig. 6**, a vortical cavity is evident in the vicinity of the orifice outlet for CN≥4.0. Similar to **Fig. 8**, the frequency spectrum obtained by the FFT of the cavity-radius waveform is depicted in **Fig. 9**. It is evident that the spectrum corresponds to a chaotic oscillation for CN=4.0 (**Fig. 9a**). The low vapour-presence probability values in the region, as depicted in the inset of **Fig. 9a**, suggest that the cavity and consequently, the magnitude of the underlying longitudinal vortex decay occasionally. The spectrum therefore exhibits no characteristic frequencies. Nevertheless, the spectrum for CN=6.0 (**Fig. 9b**) does exhibit a dominant frequency at 883 Hz indicating that the underlying vortex gains in coherence and retains a more consistent magnitude, which reflects to a regular oscillation of the cavity radius.

Comparison of the peak frequencies of **Figs. 8b** and **9b** makes clear that the variation of the cloud-cavity topology, owing, in essence, to flow separation or cross-flow vorticity, constitutes a much more dynamic process compared to the variance in the topology of vortical cavities stemming from stream-wise vortical motion. A secondary peak at around 2,104 Hz can also be discerned in **Fig. 9b**, which could be attributed to perturbations induced by the closure region of the cloud cavity, as there is a certain level of overlap between the two regimes within the orifice, as highlighted in **Fig. 4a**.

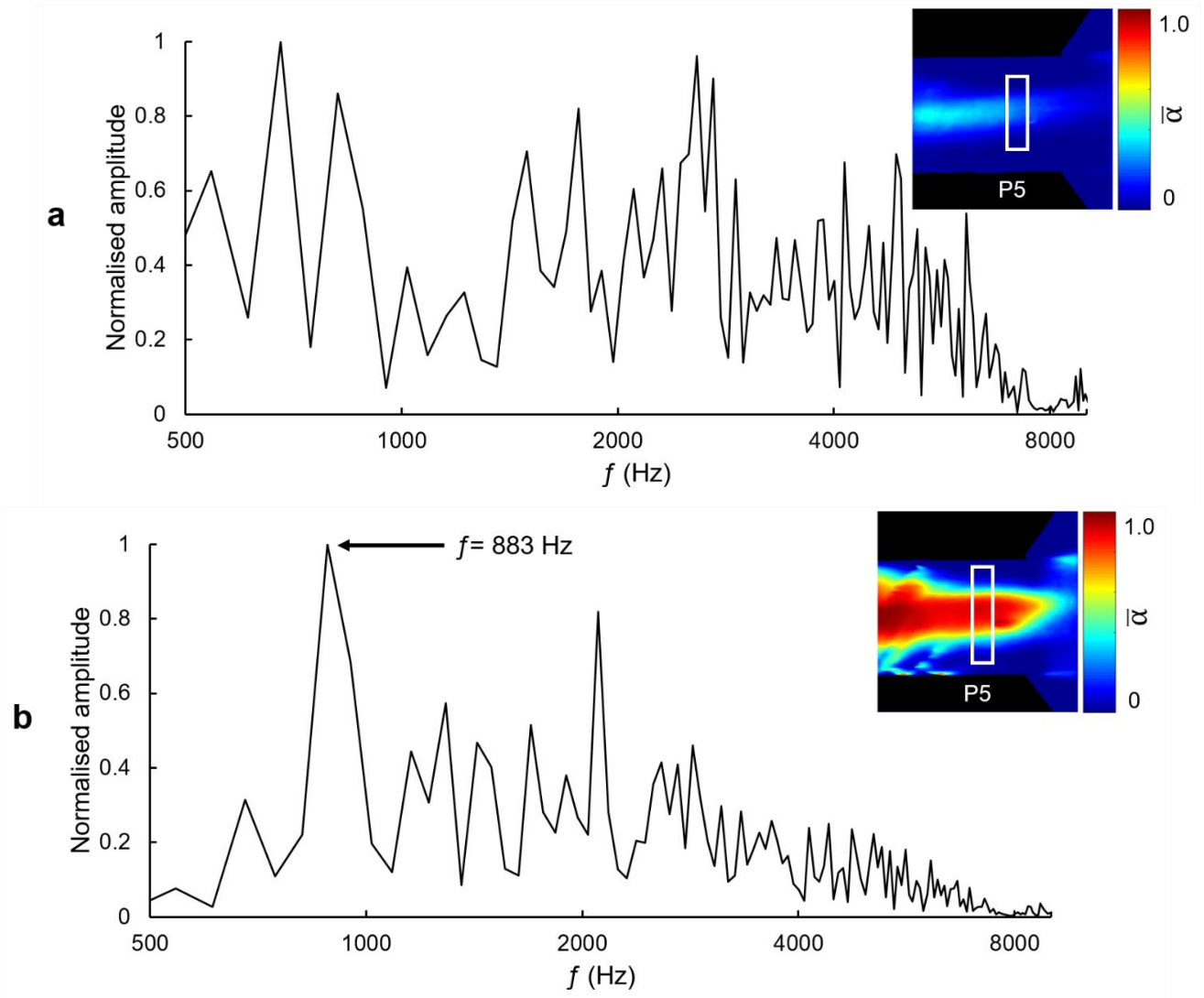

Fig. 9 Frequency spectrum of vortical-cavity radius fluctuations obtained through FFT (Lift=0.5 mm): (a) CN=4.0 and (b) CN=6.0. The diameter of the vortical cavity is calculated by averaging along a control window (white rectangle area) shown in conjunction with the vapour presence probability contour plot, in the insets of the two panels.

4.2 Quantification of in-nozzle vapour content

Time resolved-absorption measurements provide a representative 2-D projection of the two-phase flow field, yet containing integrated information in terms of vapour content along the line-of-sight; hence, an interpretation of the volumetric topology of vapour structures can be facilitated. A tomographic visualisation with current CT state-of-the-art is practically infeasible due to the extremely small timescales of flow-processes evolution. In other words, each pixel-brightness value in the resulting image represents an ensemble of all beam interactions with vapour structures, perpendicular to the viewing plane. The temporal evolution of vapour path obtained through absorption imaging at the orifice inlet is illustrated in **Fig. 10**. These time-resolved, quantitative results, offer further information regarding the actual vapour content of the cloud and vortical cavities

detected in the XPCI experiment. Even from the sequence of few radiographs shown in **Fig. 10**, it is clearly discernible that the central region of the cloud cavity, although it is quite stable, does not correspond to significant vapour quantities. It becomes therefore evident that qualitative techniques such as XPCI and predominantly visible-light methods, where scattering/refraction phenomena are more intense, fail to capture the actual volumetric vapour content, as has also been verified for much more stable flows [16,20,25,38].

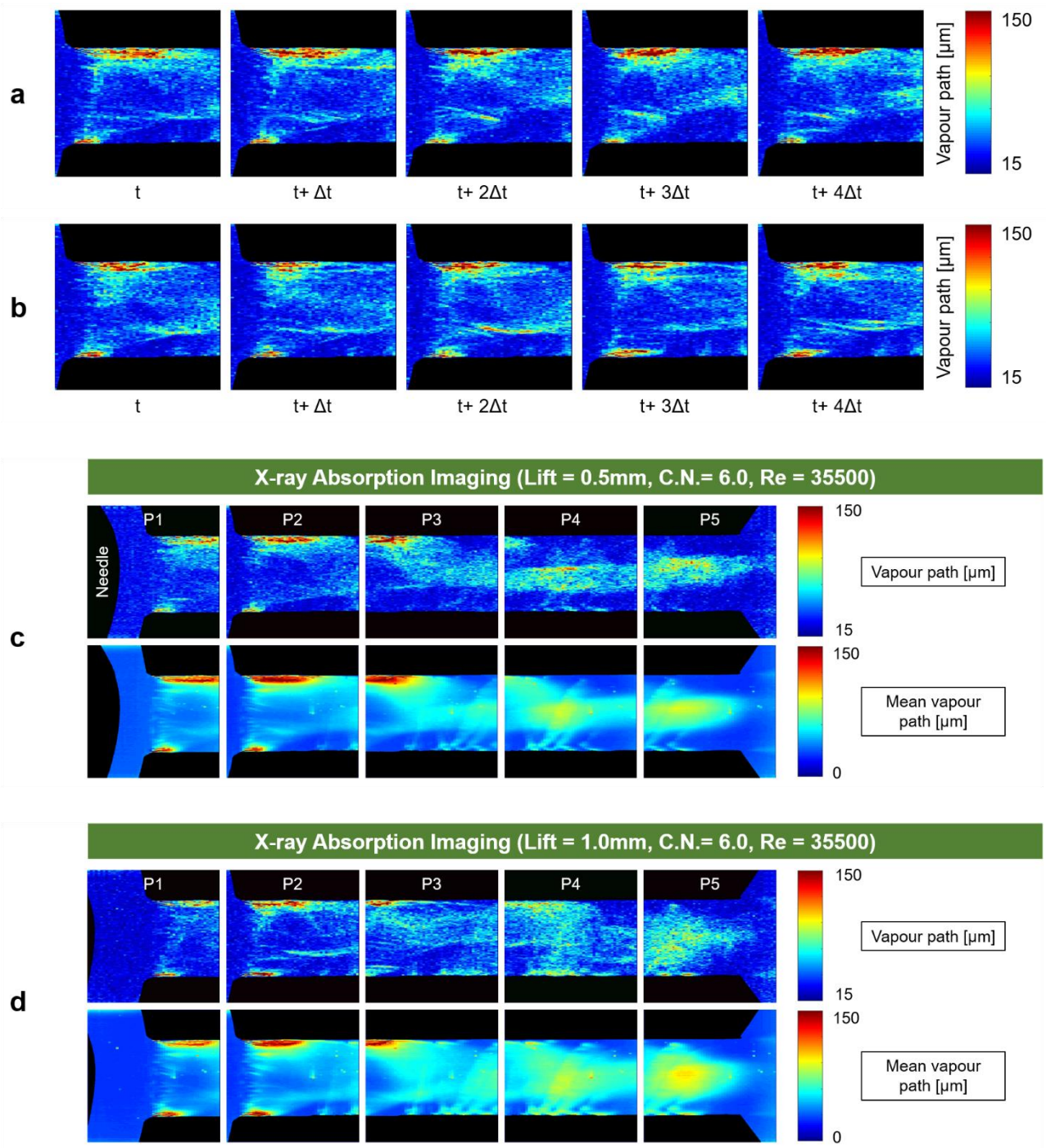

Fig. 10 Contour plots of the temporal evolution of projected vapour path at the orifice inlet, as obtained through absorption imaging: (a) Lift=0.5, CN=6.0, P2 (orifice entrance) and (b) Lift=1.0, CN=6.0, P2 (orifice entrance). Animations depicting a series of times instances are provided as supplementary movies for (c) L=0.5, CN=6.0 (Multimedia view) and (d) L=1.0, CN=6.0 (Multimedia view).

As described earlier, a set of 5,000 radiographs were processed in every panel of the orifice for all the test cases examined; the mean vapour path is illustrated in **Fig. 11**. The same flow conditions as

in the XPCI experiment were recreated for the absorption measurements. However, results for the low CN case (=2.0) could not be obtained as the signal-to-noise ratio was not strong enough to extract meaningful physical information. Referring to CN=4.0 (**Fig. 11a**), asymmetrical cavities can be detected attached to the orifice wall with high vapour content, i.e. with mean vapour-path values of approximately 180 μm or 64% of the local orifice cross-section chord. In agreement with the XPCI findings, the upper projected cavity appears to be more extensive in size compared to the lower one due to flow asymmetry, as discussed in the previous section. Nevertheless, both panels of **Fig. 11** demonstrate that the vapour content at the projected orifice core is rather low, i.e. the mean vapour path values are of the order of 55 μm, corresponding to 4% of the local orifice chord. Juxtaposition of the XPCI and absorption data of **Figs 6a** and **11**, suggests that a sheet of vapour is attached at the orifice circumference yet its core is occupied mainly by liquid and, thus the projected vapour-path values are low. A similar 'halo' effect has been detected by X-ray imaging in similar geometries, as the generated vapour follows the orifice curvature and forms a torus [13,39]. It therefore becomes, once again evident that qualitative methods are susceptible to exaggerating the vapour content of wall-bounded cavitating flows.

The absorption data verify the main conclusions derived by XPCI, regarding the effect of needle lift on cavitation evolution. Elongated vortical cavities are more pronounced in the low needle-lift case, whereas a more extensive cavity shedding sequence seems to be the prevailing regime for high lift. Nevertheless, the quantitative data also reveal that the two attached vapour pockets at the orifice entrance contain different amounts of vapour. For the low CN cases (**Fig. 11a**), only few transient structures persist beyond P3, with the mean vapour path values being of the order of 30 μm for both lifts. Significantly higher vapour-path values can be observed as CN increases (**Fig. 11b**). Firstly, the cavities of high vapour content, which are attached at the sidewall in the orifice entrance region, grow in size. Besides, as CN increases in the low needle-lift cases, vapour content by partial-cavity shedding merges into the vortical cavity; the absorption results highlight this overlap, refer especially to P3 of the contour plot corresponding to Lift=0.5 and CN=6.0. It is interesting to notice that in P3-P5, cavities emanating due to local imperfections of the sidewall are being entrained by the main flow-stream and coalesce with the shed or vortical cavities leading to local peaks of the vapour path.

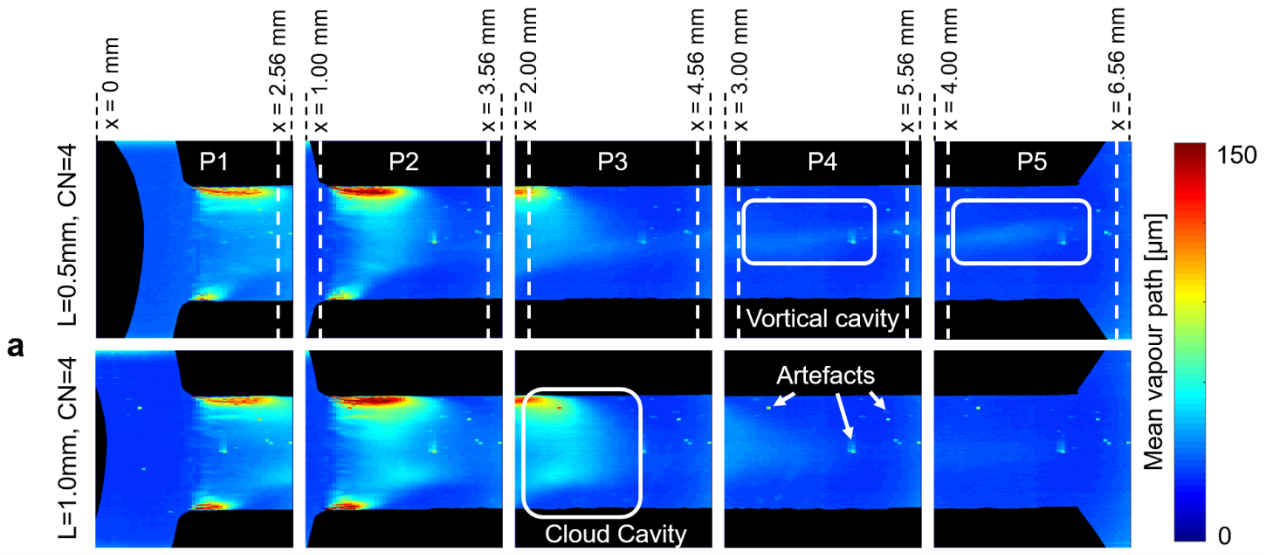

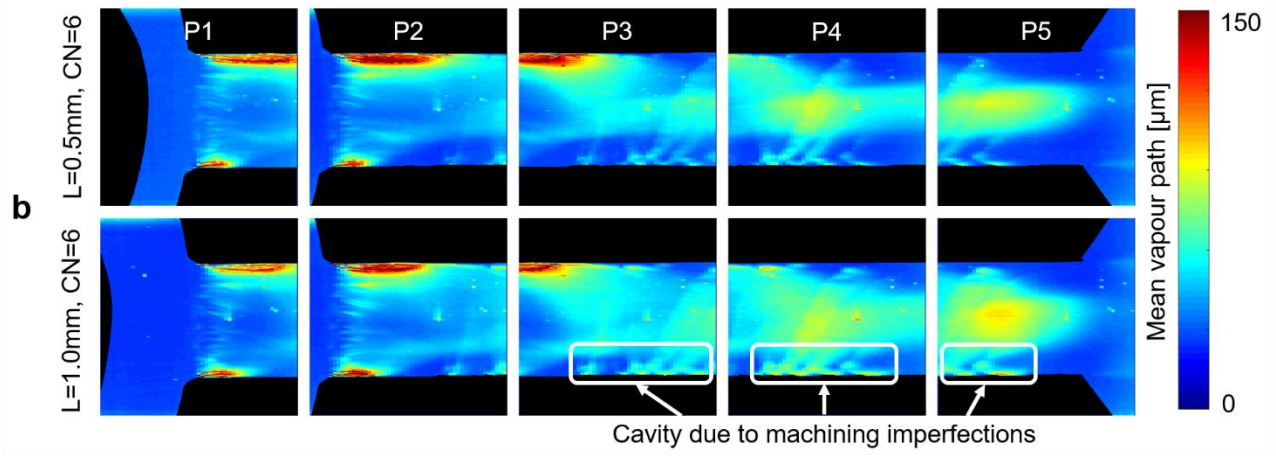

Fig. 11 Contour plots of the time-averaged vapour content and for different flow conditions, as obtained by absorption imaging: (a) CN=4.0 and (b) CN=6.0.

Mean-vapour path values obtained in the five irradiated panels for all the examined flow conditions are shown in **Fig. 12**, in order to evaluate the variation of the overall extent of vapour along the orifice length. The rationale is similar to that of **Fig. 7** concerning XPCI data and the positions of the irradiation panels are identical to those shown in **Fig. 7c**. It is discernible that higher CN cases exhibit more extensive vapour formation in all cases, as expected. With reference to the low CN cases, increasing the needle lift, results in increase of the overall vapour content within the orifice. Higher needle lift favours the more extensive cloud cavitation regime over the more localised vortical cavitation. A trend that is corroborated by the high CN cases as well. An exception is noted for P1 of the CN=6.0 case, where increase of the needle lift leads to a slight reduction of the mean vapour-path value in the characteristic region. This behaviour is primarily influenced by the vapour quantity in the attached pockets in the orifice entrance, setting in due to the post-constriction flow separation. This separation is expected to be more violent and hence leading to more significant phase change for low needle lift, i.e. high flow blockage ratio [48].

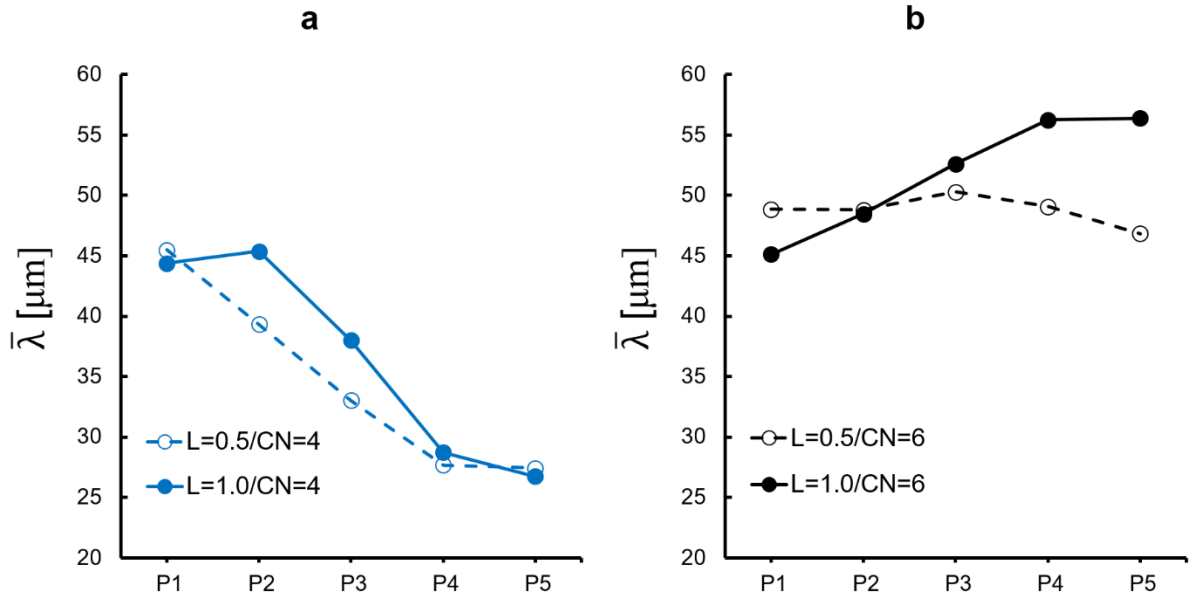

Fig. 12 Temporally- and spatially-averaged values of vapour path $\bar{\lambda}$ for (a) CN=4.0 and (b) CN=6.0 along the irradiated panels. Graph values have been calculated by spatially averaging the range of vapour-path values obtained in each characteristic location of the contour plots of **Fig. 11,** excluding the low signal-to-noise regions.

Finally, a comparative assessment of the two techniques is of essence to underpin the physical information that can be extracted by each one of them. XPCI is a powerful visualisation technique providing faithful representation of highly perturbed and rapidly varying interfaces, as demonstrated in **Fig. 6**. Hence, it is capable of providing quantitative information on cavitation dynamics. However, the comparison of average two-phase flow field representations by XPCI (**Fig. 6a**) and absorption imaging (**Fig. 11**) reveals that the qualitative method obscures the magnitude of distinct structures in complex cavitation regimes, as it does not give any insight on the 'depth' of the structures. In other words, a stable thin film cavity would be represented in the same way as a well-established cloud occupying the entire orifice core, in terms of vapour-presence probability. Such limitations are alleviated by absorption imaging that clearly illustrates the extent of structures along the line-of-sight dimension. An illustrative example regarding potential pitfalls of qualitative techniques is given in **Fig. 13a**, where results concerning both implemented techniques are shown. For instance, regarding the most complex cavitation topology arising in the examined cases (Lift=1.0, CN=6.0), the mean vapour probability is shown to be decreasing along the orifice length, while the vapour content values exhibit the opposite trend (**Fig. 13b**). In other words, although in reality the vaporous structures gain in coherence along the line-of-sight dimension, an interpretation based on merely XPCI would suggest an opposite decaying trend. A similar remark can be made for the case characterised by CN=6.0 and needle lift of 0.5 mm. As seen in **Fig. 13b** for the specific case, the presence probability undergoes a decrease along the orifice length, whereas the respective path values remain almost constant. Both cases facilitate the conclusion that in cavitation regimes, where attached and transient cavities coexist, estimations on the in-nozzle vapour content based on qualitative data could be misleading, as a shift in the cavity morphology could be perceived as reduction in its vapour quantity. Although only line-of-sight techniques were evaluated in the present investigation, the projected qualitative and quantitative data can be utilised to enable the apprehension of the three-dimensional topology of cavitating structures. **Fig. 13c** illustrates a CFD-based conceptual representation of co-existing attached and vortical cavitation. The asymmetrical topology of the cloud, once projected onto a 2-D plane would result to the asymmetrical vapour pockets with high mean vapour-path values evident in **Fig. 13a**. Moreover, any transient structures forming in the orifice core, either string or shed cavities, also contribute to the ensemble vapour-path values along the line of sight, leading to high vapour-path values further downstream the orifice length and closer to the outlet region.

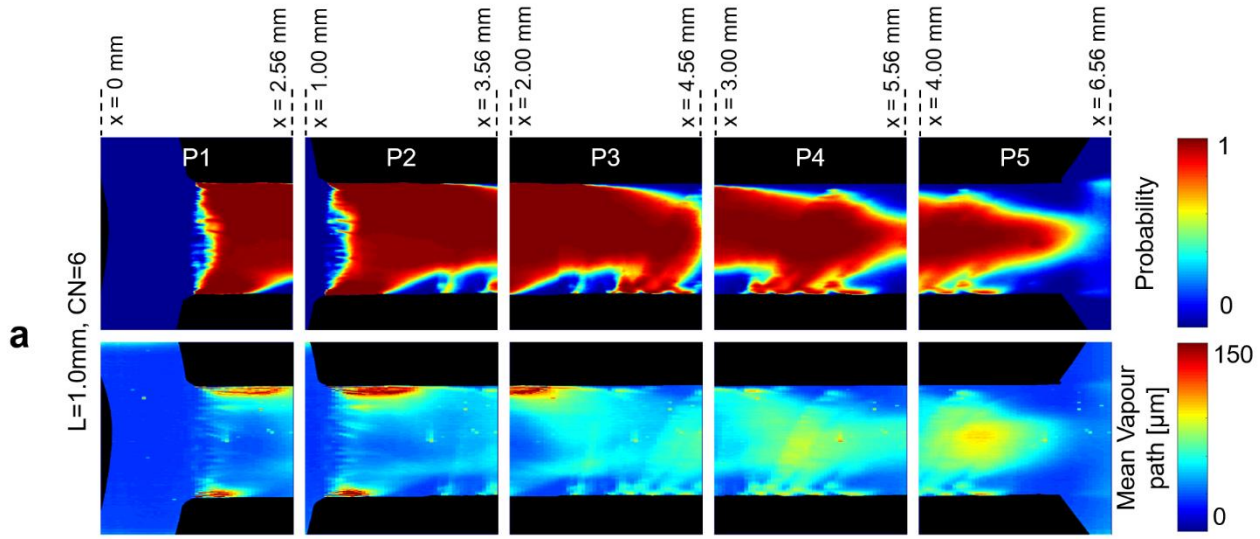

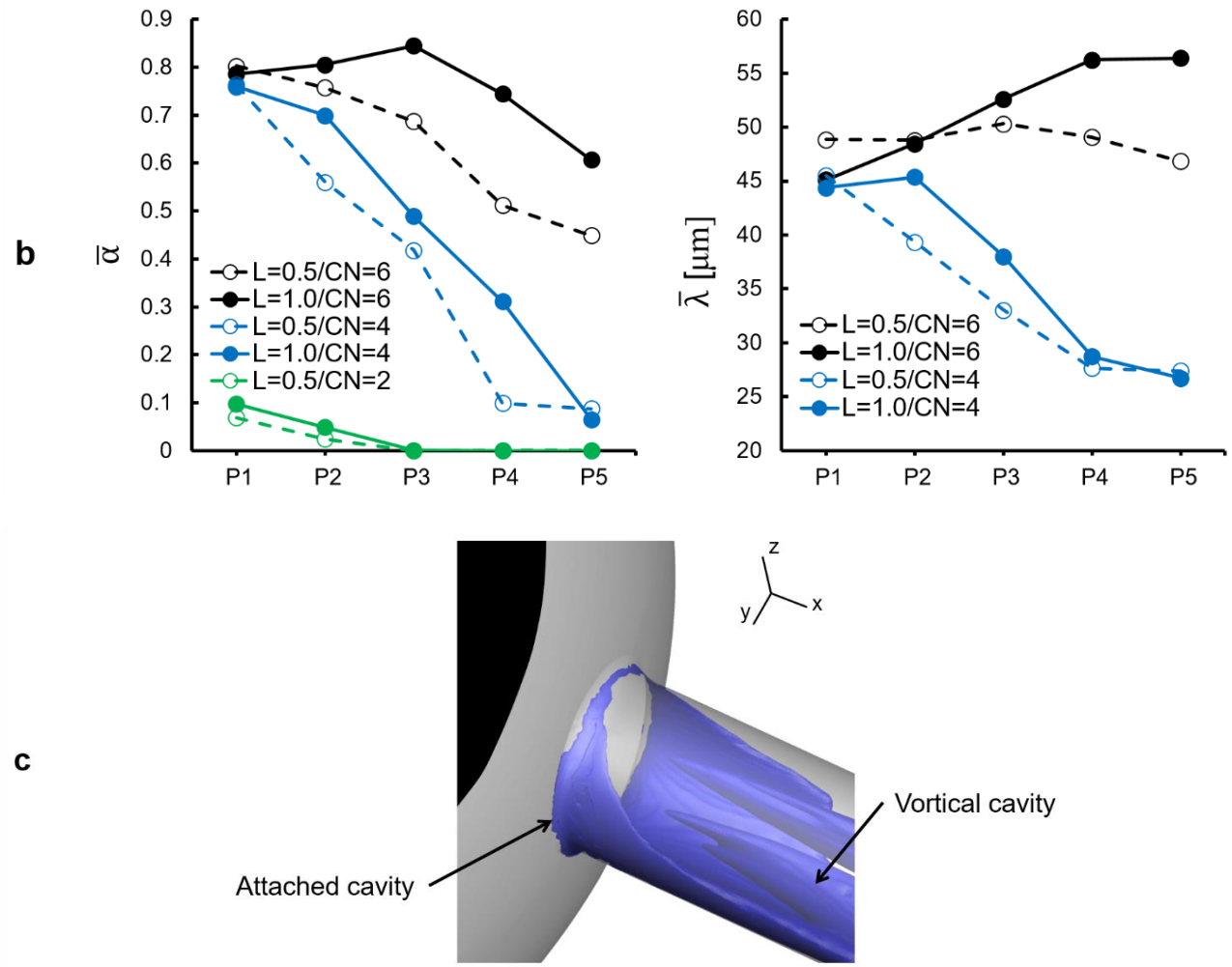

Fig. 13 Comparison between qualitative and quantitative data: (a) Contour plots of the vapour-presence probability $\bar{\alpha}$ and mean vapour path $\bar{\lambda}$ for Lift=1.0, CN=6.0 and (b) respective averaged-value distributions along the orifice length. (c) Conceptual three-dimensional cavitation topology in the orifice entrance encompassing attached and vortical cavities.

Information on the dynamics of the transient cavitating flow can also be extracted by the obtained absorption data. A space-time representation of the projected vapour-path values corresponding to the cavities attached to the orifice wall in the entrance region is shown in **Fig. 14**. Since the cavity projection creates two distinct regions of high vapour-path values, the data were sampled along two stream-wise lines in the vicinity of the nozzle wall, as shown in the inset of **Fig. 14.** A comparative assessment of the contour plots corresponding to the lower (C1) and upper (C2) projected cavities reveals that the former exhibits higher vapour-path peak values and a more localised topology compared to the latter. Furthermore, the lower projected cavity is located closer to the orifice entrance and its extent varies more significantly with time. It has to be emphasised that, in reality, the two projected vapour pockets are encompassed in the same three-dimensional partial cavity. The cross-flow vortical system induced by the flow separation past the constriction constitutes the underlying cause for the cavity formation. The observed asymmetry therefore suggests that the cross-flow separation vortex has a laterally varying magnitude and, thus, it is expected to give rise to a span-wise pressure gradient leading to chaotic shedding of structures locally, i.e. in the orifice entrance region shown in the inset of **Fig. 14**. This postulation is in agreement with the form of the succession of low/high vapour-path values in the spatio-temporal diagram, which has a horizontal orientation. As also pointed out by Barbaca et al. [25], presence of a re-entrant jet would shift the streaks to a

downward slope, while cavities exhibiting the reported 'non-auto oscillating' behaviour are characterised by horizontal streaks.

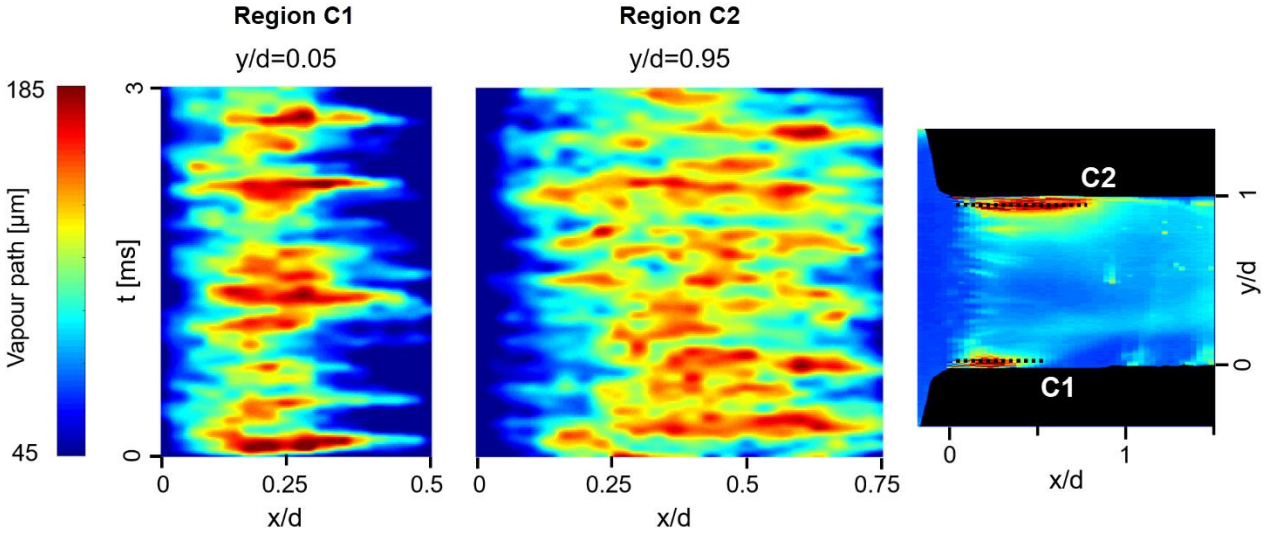

Fig.14 Spatio-temporal evolution of the vapour path at characteristic locations (dashed lines in the inset of the figure) of the attached vapour pockets. The inset corresponds to the irradiation panel in the vicinity of the orifice inlet (P2) and the contour plots presented correspond to flow conditions characterised by Lift=1.0mm and CN=6.0 .

5. Conclusions

The capability of synchrotron-radiation imaging to quantify in a time-resolved manner the dynamic evolution of highly-transient, wall-bounded cavitating flows has been demonstrated. A combination of X-ray phase-contrast and absorption line-of-sight imaging has been evaluated to elucidate the morphology and vapour content of different cavitation regimes arising within a cylindrical orifice with an abruptly constricted flow path. Depending on the lift of the metallic needle (0.5 or 1.0 mm) constricting the flow, transient features associated with either cloud or vortical cavitation were found to be more prevalent, although both regimes within the orifice co-existed regardless of the lift value.

XPCI radiographs exhibit a sharp contrast at the interface region, thus providing the means to capture the temporal variation of fine features of transient vaporous structures. In turn, this enables the identification of fundamental mechanisms governing cavitation development. Shedding of coherent structures from the trailing edge of the attached cavity was demonstrated to be the distinct transient feature for lift of 1.0 mm and well-established cavitation (CN≥4.0). The range of Strouhal numbers characterising the shedding sequence, suggested it was governed by a re-entrant jet motion. For the lower needle-lift case examined (0.5 mm), an elongated vortical cavity was found to establish throughout the orifice length, once again for CN≥4.0. The cavity radius fluctuation could be tracked over time using XPCI and its characteristic frequency revealed that the underlying vortex obtains a relatively steady recirculation magnitude only for CN=6.0.

Absorption imaging was proven capable of quantifying the vapour extent of both steady and time-variant cavities forming within the orifice. High vapour-path values were detected only in the asymmetrical vapour pockets attached close the orifice entrance. In contrast, the orifice core was occupied by moderate quantities of vapour even for the highest CN examined (=6.0), despite the fact that the XPCI data verified vapour-presence values close to unity in the region. Concurrent assessment of qualitative and quantitative projected data enabled the interpretation of the 3-D cavitation topology, as an asymmetrical cloud attaching across the orifice periphery, whereas the core is mostly occupied by liquid. Transient elongated cavities overlap those shed from the closure region of the attached cavities, leading to increase of the vapour-path length towards the outlet. Besides, it has been verified that high vapour-presence probabilities do not necessarily indicate large vapour

quantities. Namely, a thin cloud exhibits more extensive vapour presence throughout the orifice cross-section than a localised string cavity, yet the opposite trend occurs regarding vapour-path values. The temporally-resolved vapour-path values illustrated that the extent of the vapour pockets attached at the entrance region exhibits an oscillating behaviour, yet, unlike the closure region, periodic shedding was not detected. Overall, the investigation has highlighted the advantages of employing X-ray attenuation and phase shift to obtain qualitative and quantitative information in a non-invasive manner in complex and transient cavitation patterns were optical imaging fails due to excessive light scattering.

Supplementary Material
Animations of time-resolved XPCI and absorption-imaging data are offered as supplementary material.

Acknowledgments
Funding for this research has been provided by the EU Horizon-2020 Marie Skłodowska-Curie Global Fellowships AHEAD (IK, Grant No. 794831) and UNIFIED (PK, Grant No. 748784), through which the international visiting program of Ioannis K. Karathanassis and Phoevos Koukouvinis at the Sandia National Laboratories was supported. Sandia National Laboratories is a multi-mission laboratory managed and operated by National Technology and Engineering Solutions of Sandia, LLC., a wholly owned subsidiary of Honeywell International, Inc., for the U.S. Department of Energy's National Nuclear Security Administration under contract DE-NA0003525. Additional funding has been received by the UK's Engineering and Physical Sciences Research Council (EPSRC) through grant EP/K020846/1. This research also used resources of the Advanced Photon Source, a U.S. Department of Energy (DOE) Office of Science User Facility operated for the DOE Office of Science by Argonne National Laboratory under Contract No. DE-AC02-06CH11357.

Data Availability Statement
Raw data were generated at the Advanced Photon Source, a large-scale facility of the Argonne National Laboratory. Data supporting the findings of this study are available as supplementary material. Further derived data are available from the corresponding author upon reasonable request.

References

[1] Šarc, A., Kosel, J., Stopar, D., Oder, M., and Dular, M., 2018, "Removal of Bacteria Legionella Pneumophila, Escherichia Coli, and Bacillus Subtilis by (Super)Cavitation," Ultrason. Sonochem., **42**, pp. 228–236.

[2] Qian, J. yuan, Gao, Z. xin, Hou, C. wei, and Jin, Z. jiang, 2019, "A Comprehensive Review of Cavitation in Valves: Mechanical Heart Valves and Control Valves," Bio-Design Manuf., **2**(2), pp. 119–136.

[3] Lohse, D., 2018, "Bubble Puzzles: From Fundamentals to Applications," Phys. Rev. Fluids, **3**(11), pp. 1–42.

[4] Peters, A., Lantermann, U., and el Moctar, O., 2018, "Numerical Prediction of Cavitation Erosion on a Ship Propeller in Model- and Full-Scale," Wear, **408**–**409**, pp. 1–12.

[5] Hao, Y., and Tan, L., 2018, "Symmetrical and Unsymmetrical Tip Clearances on Cavitation Performance and Radial Force of a Mixed Flow Pump as Turbine at Pump Mode," Renew. Energy, **127**, pp. 368–376.

[6] Shimpi, N., Mali, A., Hansora, D. P., and Mishra, S., 2015, "Synthesis and Surface Modification of Calcium Carbonate Nanoparticles Using Ultrasound Cavitation Technique," Nanosci. Nanoeng., **3(1)**, pp. 8–12.

[7] Chen, Z., He, Z., Shang, W., Duan, L., Zhou, H., Guo, G., and Guan, W., 2018, "Experimental Study on the Effect of Nozzle Geometry on String Cavitation in Real-Size Optical Diesel Nozzles and Spray Characteristics," Fuel, **232**, pp. 562–571.

[8] Krivokorytov, M. S., Zeng, Q., Lakatosh, B. V., Vinokhodov, A. Y., Sidelnikov, Y. Y., Kompanets, V. O., Krivtsun, V. M., Koshelev, K. N., Ohl, C. D., and Medvedev, V. V., 2018, "Shaping and Controlled Fragmentation of Liquid Metal Droplets through Cavitation," Sci. Rep., **8**(1), p. 597.

[9] Adamkowski, A., Henke, A., and Lewandowski, M., 2016, "Resonance of Torsional Vibrations of Centrifugal Pump Shafts Due to Cavitation Erosion of Pump Impellers," Eng. Fail. Anal., **70**, pp. 56–72.
[10] Li, Y., Feng, G., Li, X., Si, Q., and Zhu, Z., 2018, "An Experimental Study on the Cavitation Vibration Characteristics of a Centrifugal Pump at Normal Flow Rate," J. Mech. Sci. Technol., **32**(10), pp. 4711–4720.
[11] Aktas, B., Atlar, M., Turkmen, S., Shi, W., Sampson, R., Korkut, E., and Fitzsimmons, P., 2016, "Propeller Cavitation Noise Investigations of a Research Vessel Using Medium Size Cavitation Tunnel Tests and Full-Scale Trials," Ocean Eng., **120**, pp. 122–135.
[12] Wittekind, D., and Schuster, M., 2016, "Propeller Cavitation Noise and Background Noise in the Sea," Ocean Eng., **120**, pp. 116–121.
[13] Koukouvinis, P., Mitroglou, N., Gavaises, M., Lorenzi, M., and Santini, M., 2017, "Quantitative Predictions of Cavitation Presence and Erosion-Prone Locations in a High-Pressure Cavitation Test Rig," J. Fluid Mech., **819**, pp. 21–57.
[14] Dular, M., and Petkovšek, M., 2015, "On the Mechanisms of Cavitation Erosion - Coupling High Speed Videos to Damage Patterns," Exp. Therm. Fluid Sci., **68**, pp. 359–370.
[15] Mithun, M. G., Koukouvinis, P., and Gavaises, M., 2018, "Numerical Simulation of Cavitation and Atomization Using a Fully Compressible Three-Phase Model," Phys. Rev. Fluids, **3**(6), p. 064304.
[16] Ganesh, H., Mäkiharju, S. A., and Ceccio, S. L., 2016, "Bubbly Shock Propagation as a Mechanism for Sheet-to-Cloud Transition of Partial Cavities," J. Fluid Mech., **802**, pp. 37–78.
[17] Mäkiharju, S. A., Ganesh, H., and Ceccio, S. L., 2017, "The Dynamics of Partial Cavity Formation, Shedding and the Influence of Dissolved and Injected Non-Condensable Gas," J. Fluid Mech., **829**, pp. 420–458.
[18] Barwey, S., Ganesh, H., Hassanaly, M., Raman, V., and Ceccio, S., 2020, "Data-Based Analysis of Multimodal Partial Cavity Shedding Dynamics," Exp. Fluids, **61**(4), pp. 1–21.
[19] Kravtsova, A. Y., Markovich, D. M., Pervunin, K. S., Timoshevskiy, M. V., and Hanjalić, K., 2014, "High-Speed Visualization and PIV Measurements of Cavitating Flows around a Semi-Circular Leading-Edge Flat Plate and NACA0015 Hydrofoil," Int. J. Multiph. Flow, **60**, pp. 119–134.
[20] Wu, J., Ganesh, H., and Ceccio, S., 2019, "Multimodal Partial Cavity Shedding on a Two-Dimensional Hydrofoil and Its Relation to the Presence of Bubbly Shocks," Exp. Fluids, **60**(4), pp. 1–17.
[21] Foeth, E. J., van Doorne, C. W. H., van Terwisga, T., and Wieneke, B., 2006, "Time Resolved PIV and Flow Visualization of 3D Sheet Cavitation," Exp. Fluids, **40**(4), pp. 503–513.
[22] Stutz, B., and Legoupil, S., 2003, "X-Ray Measurements within Unsteady Cavitation," Exp. Fluids, **35**(2), pp. 130–138.
[23] Gavaises, M., Andriotis, A., Papoulias, D., Mitroglou, N., and Theodorakakos, A., 2009, "Characterization of String Cavitation in Large-Scale Diesel Nozzles with Tapered Holes," Phys. Fluids, **21**(5), p. 052107.
[24] Jahangir, S., Wagner, E. C., Mudde, R. F., and Poelma, C., 2019, "Void Fraction Measurements in Partial Cavitation Regimes by X-Ray Computed Tomography," Int. J. Multiph. Flow, **120**, p. 103085.
[25] Barbaca, L., Pearce, B. W., Ganesh, H., Ceccio, S. L., and Brandner, P. A., 2019, "On the Unsteady Behaviour of Cavity Flow over a Two-Dimensional Wall-Mounted Fence," J. Fluid Mech., **874**, pp. 483–525.
[26] Saito, Y., and Sato, K., 2003, "Cavitation Bubble Collapse and Impact in the Wake of a Circular Cylinder," Mater. Sci.
[27] Kumar, P., Chatterjee, D., and Bakshi, S., 2017, "Experimental Investigation of Cavitating Structures in the near Wake of a Cylinder," Int. J. Multiph. Flow, **89**, pp. 207–217.

[28] Wang, Y., Xu, C., Wu, X., Huang, C., and Wu, X., 2017, "Ventilated Cloud Cavitating Flow around a Blunt Body Close to the Free Surface," Phys. Rev. Fluids, **2**(8), p. 084303.
[29] Trummler, T., Schmidt, S. J., and Adams, N. A., 2020, "Investigation of Condensation Shocks and Re-Entrant Jet Dynamics in a Cavitating Nozzle Flow by Large-Eddy Simulation," Int. J. Multiph. Flow, **125**, p. 103215.
[30] Brunhart, M., Soteriou, C., Gavaises, M., Karathanassis, I., Koukouvinis, P., Jahangir, S., and Poelma, C., 2020, "Investigation of Cavitation and Vapor Shedding Mechanisms in a Venturi Nozzle," Phys. Fluids, **32**(8), p. 083306.
[31] Choi, J., and Ceccio, S. L., 2007, "Dynamics and Noise Emission of Vortex Cavitation Bubbles," J. Fluid Mech., **575**(2007), pp. 1–26.
[32] Choi, J., Hsiao, C.-T., Chahine, G., and Ceccio, S., 2009, "Growth, Oscillation and Collapse of Vortex Cavitation Bubbles," J. Fluid Mech., **624**(2009), pp. 255–279.
[33] Kastengren, A., and Powell, C. F., 2014, "Synchrotron X-Ray Techniques for Fluid Dynamics," Exp. Fluids, **55**(3), pp. 1–15.
[34] Heindel, T. J., 2011, "A Review of X-Ray Flow Visualization With Applications to Multiphase Flows," J. Fluids Eng., **133**(7), p. 074001.
[35] Heindel, T. J., 2018, "X-Ray Imaging Techniques to Quantify Spray Characteristics in the near Field," At. Sprays, **28**(11), pp. 1029–1059.
[36] Coutier-Delgosha, O., Stutz, B., Vabre, A., and Legoupil, S., 2007, "Analysis of Cavitating Flow Structure by Experimental and Numerical Investigations," J. Fluid Mech., **578**, p. 171.
[37] Aeschlimann, V., Barre, S., and Legoupil, S., 2011, "X-Ray Attenuation Measurements in a Cavitating Mixing Layer for Instantaneous Two-Dimensional Void Ratio Determination," Phys. Fluids, **23**(5), p. 055101.
[38] Mäkiharju, S. A., Gabillet, C., Paik, B.-G., Chang, N. A., Perlin, M., and Ceccio, S. L., 2013, "Time-Resolved Two-Dimensional X-Ray Densitometry of a Two-Phase Flow Downstream of a Ventilated Cavity," Exp. Fluids, **54**(7), p. 1561.
[39] Mitroglou, N., Lorenzi, M., Santini, M., and Gavaises, M., 2016, "Application of X-Ray Micro-Computed Tomography on High-Speed Cavitating Diesel Fuel Flows," Exp. Fluids, **57**(11), p. 175.
[40] Bauer, D., Barthel, F., and Hampel, U., 2018, "High-Speed x-Ray CT Imaging of a Strongly Cavitating Nozzle Flow," J. Phys. Commun., **2**(7), p. 075009.
[41] Dash, A., Jahangir, S., and Poelma, C., 2018, "Direct Comparison of Shadowgraphy and X-Ray Imaging for Void Fraction Determination," Meas. Sci. Technol., **29**(12), p. 125303.
[42] Duke, D. J., Kastengren, A. L., Tilocco, F. Z., Swantek, A. B., and Powell, C. F., 2013, "X-Ray Radiography Measurements of Cavitating Nozzle Flow," At. Sprays, **23**(9), pp. 841–860.
[43] Zhang, G., Khlifa, I., Fezzaa, K., Ge, M., and Coutier-Delgosha, O., 2020, "Experimental Investigation of Internal Two-Phase Flow Structures and Dynamics of Quasi-Stable Sheet Cavitation by Fast Synchrotron x-Ray Imaging," Phys. Fluids, **32**(11), p. 113310.
[44] Karathanassis, I. K., Koukouvinis, P., Kontolatis, E., Lee, Z., Wang, J., Mitroglou, N., and Gavaises, M., 2018, "High-Speed Visualization of Vortical Cavitation Using Synchrotron Radiation," J. Fluid Mech., **838**, pp. 148–164.
[45] Moon, S., Huang, W., and Wang, J., 2019, "First Observation and Characterization of Vortex Flow in Steel Micronozzles for High-Pressure Diesel Injection," Exp. Therm. Fluid Sci., **105**, pp. 342–348.
[46] Tekawade, A., Sforzo, B. A., Matusik, K. E., Fezzaa, K., Kastengren, A. L., and Powell, C. F., 2020, "Time-Resolved 3D Imaging of Two-Phase Fluid Flow inside a Steel Fuel Injector Using Synchrotron X-Ray Tomography," Sci. Rep., **10**(1), pp. 1–9.
[47] Kasa, M., Borland, M., Emery, L., Fuerst, J., Harkay, K. C., Hasse, Q., Ivanyushenkov, Y., Jansma, W., Kesgin, I., Sajaev, V., Shiroyanagi, Y., Sun, Y. P., and Gluskin, E., 2020, "Development and Operating Experience of a 1.2-m Long Helical Superconducting Undulator at the Argonne Advanced Photon Source," Phys. Rev. Accel. Beams, **23**(5), p.

050701.
[48] Karathanassis, I. K., Trickett, K., Koukouvinis, P., Wang, J., Barbour, R., and Gavaises, M., 2018, “Illustrating the Effect of Viscoelastic Additives on Cavitation and Turbulence with X-Ray Imaging,” Sci. Rep., **8**(1), p. 14968.
[49] Kolev, N., 2007, *Multiphase Flow Dynamics: Fundamentals*, Springer.
[50] Kovesi, P., 1995, “Image Features from Phase Congruency,” Tech. Report, Univ. West. Aust., **95/4**.
[51] Otsu, N., 1979, “A Threshold Selection Method from Gray-Level Histograms,” IEEE Trans. Syst. Man Cybern., **9**(1).
[52] Als-Nielsen, J., and McMorrow, D., 2011, *Elements of Modern X-Ray Physics*, Wiley.
[53] Russo, P., 2014, “Physical Basis of X-Ray Imaging,” *Comprehensive Biomedical Physics*, Elsevier, pp. 1–48.
[54] Battistoni, M., Duke, D. J., Swantek, A. B., Tilocco, F. Z., Powell, C. F., and Som, S., 2015, “Effects of Noncondensable Gas on Cavitating Nozzles,” At. Sprays, **25**(6), pp. 453–483.
[55] Duke, D. J., Kastengren, A. L., Swantek, A. B., Matusik, K. E., and Powell, C. F., 2016, “X-Ray Fluorescence Measurements of Dissolved Gas and Cavitation,” Exp. Fluids, **57**(10), p. 162.
[56] Moffat, R. J., 1988, “Describing the Uncertainties in Experimental Results,” Exp. Therm. Fluid Sci., **1**(1), pp. 3–17.
[57] Franc, J.-P., and Michel, J.-M., 2004, *Fundamentals of Cavitation*, Kluwer Academic Publishers.
[58] Sato, K., and Saito, Y., 2002, “Unstable Cavitation Behavior in a Circular-Cylindrical Orifice Flow.,” JSME Int. J. Ser. B, **45**(3), pp. 638–645.
[59] Arndt, R. E. A., 2002, “Cavitation in Vortical Flows,” Annu. Rev. Fluid Mech., **34**, pp. 143–175.